

# Measurement of the production cross-section of positive pions in the collision of 8.9 GeV/c protons on beryllium

M.G. Catanesi<sup>1</sup>, E. Radicioni<sup>1</sup>, R. Edgecock<sup>2</sup>, M. Ellis<sup>2a</sup>, S. Robbins<sup>2b,c</sup>, F.J.P. Soler<sup>2d</sup>, C. Gößling<sup>3</sup>, S. Bunyatov<sup>4</sup>, G. Chelkov<sup>4</sup>, D. Dedovitch<sup>4</sup>, M. Gostkin<sup>4</sup>, A. Guskov<sup>4</sup>, D. Khartchenko<sup>4</sup>, A. Krasnoperov<sup>4</sup>, Z. Kroumchtein<sup>4</sup>, Y. Nefedov<sup>4</sup>, B. Popov<sup>4e</sup>, V. Serdiouk<sup>4</sup>, V. Tereshchenko<sup>4</sup>, A. Zhemchugov<sup>4</sup>, E. Di Capua<sup>5</sup>, G. Vidal-Sitjes<sup>5f,g</sup>, A. Artamonov<sup>6h</sup>, P. Arce<sup>6i</sup>, S. Giani<sup>6</sup>, S. Gilardoni<sup>6f</sup>, P. Gorbunov<sup>6h,j</sup>, A. Grant<sup>6</sup>, A. Grossheim<sup>6f,k</sup>, P. Gruber<sup>6f,l</sup>, V. Ivanchenko<sup>6m</sup>, A. Kayis-Topaksu<sup>6n</sup>, J. Panman<sup>6</sup>, I. Papadopoulos<sup>6</sup>, J. Pasternak<sup>6f</sup>, E. Tcherniaev<sup>6</sup>, I. Tsukerman<sup>6h</sup>, R. Veenhof<sup>6</sup>, C. Wiebusch<sup>6o</sup>, P. Zucchelli<sup>6j,p</sup>, A. Blondel<sup>7</sup>, S. Borghi<sup>7q</sup>, M. Campanelli<sup>7</sup>, M.C. Morone<sup>7r</sup>, G. Prior<sup>7f,s</sup>, R. Schroeter<sup>7</sup>, R. Engel<sup>8</sup>, C. Meurer<sup>8</sup>, I. Kato<sup>9k,t</sup>, U. Gastaldi<sup>10</sup>, G. B. Mills<sup>11u</sup>, J.S. Graulich<sup>12v</sup>, G. Grégoire<sup>12</sup>, M. Bonesini<sup>13</sup>, A. De Min<sup>13</sup>, F. Ferri<sup>13</sup>, M. Paganoni<sup>13</sup>, F. Paleari<sup>13</sup>, M. Kirsanov<sup>14</sup>, A. Bagulya<sup>15</sup>, V. Grichine<sup>15</sup>, N. Polukhina<sup>15</sup>, V. Palladino<sup>16</sup>, L. Coney<sup>17u</sup>, D. Schmitz<sup>17u</sup>, G. Barr<sup>18</sup>, A. De Santo<sup>18w</sup>, C. Pattison<sup>18</sup>, K. Zuber<sup>18x</sup>, F. Bobisut<sup>19</sup>, D. Gibin<sup>19</sup>, A. Guglielmi<sup>19</sup>, M. Mezzetto<sup>19</sup>, J. Dumarchez<sup>20</sup>, F. Vannucci<sup>20</sup>, V. Ammosov<sup>21</sup>, V. Koreshev<sup>21</sup>, A. Semak<sup>21</sup>, V. Zaets<sup>21</sup>, U. Dore<sup>22</sup>, D. Orestano<sup>23</sup>, F. Pastore<sup>23</sup>, A. Tonazzo<sup>23</sup>, L. Tortora<sup>23</sup>, C. Booth<sup>24</sup>, C. Buttar<sup>24f</sup>, P. Hodgson<sup>24</sup>, L. Howlett<sup>24</sup>, M. Bogomilov<sup>25</sup>, M. Chizhov<sup>25</sup>, D. Kolev<sup>25</sup>, R. Tsenov<sup>25</sup>, S. Piperov<sup>26</sup>, P. Temnikov<sup>26</sup>, M. Apollonio<sup>27</sup>, P. Chimenti<sup>27</sup>, G. Giannini<sup>27</sup>, G. Santin<sup>27y</sup>, J. Burguet-Castell<sup>28</sup>, A. Cervera-Villanueva<sup>28</sup>, J.J. Gómez-Cadenas<sup>28</sup>, J. Martín-Albo<sup>28</sup>, P. Novella<sup>28</sup>, M. Sorel<sup>28</sup>, and A. Tornero<sup>28</sup>

- <sup>1</sup> Università degli Studi e Sezione INFN, Bari, Italy
- <sup>2</sup> Rutherford Appleton Laboratory, Chilton, Didcot, UK
- <sup>3</sup> Institut für Physik, Universität Dortmund, Germany
- <sup>4</sup> Joint Institute for Nuclear Research, JINR Dubna, Russia
- <sup>5</sup> Università degli Studi e Sezione INFN, Ferrara, Italy
- <sup>6</sup> CERN, Geneva, Switzerland
- <sup>7</sup> Section de Physique, Université de Genève, Switzerland
- <sup>8</sup> Institut für Physik, Universität Karlsruhe, Germany
- <sup>9</sup> University of Kyoto, Japan
- <sup>10</sup> Laboratori Nazionali di Legnaro dell' INFN, Legnaro, Italy
- <sup>11</sup> Los Alamos National Laboratory, Los Alamos, USA
- <sup>12</sup> Institut de Physique Nucléaire, UCL, Louvain-la-Neuve, Belgium
- <sup>13</sup> Università degli Studi e Sezione INFN Milano Bicocca, Milano, Italy
- <sup>14</sup> Institute for Nuclear Research, Moscow, Russia
- <sup>15</sup> P. N. Lebedev Institute of Physics (FIAN), Russian Academy of Sciences, Moscow, Russia
- <sup>16</sup> Università "Federico II" e Sezione INFN, Napoli, Italy
- <sup>17</sup> Columbia University, New York, USA
- <sup>18</sup> Nuclear and Astrophysics Laboratory, University of Oxford, UK
- <sup>19</sup> Università degli Studi e Sezione INFN, Padova, Italy
- <sup>20</sup> LPNHE, Universités de Paris VI et VII, Paris, France
- <sup>21</sup> Institute for High Energy Physics, Protvino, Russia
- <sup>22</sup> Università "La Sapienza" e Sezione INFN Roma I, Roma, Italy
- <sup>23</sup> Università degli Studi e Sezione INFN Roma III, Roma, Italy
- <sup>24</sup> Dept. of Physics, University of Sheffield, UK
- <sup>25</sup> Faculty of Physics, St. Kliment Ohridski University, Sofia, Bulgaria
- <sup>26</sup> Institute for Nuclear Research and Nuclear Energy, Academy of Sciences, Sofia, Bulgaria
- <sup>27</sup> Università degli Studi e Sezione INFN, Trieste, Italy
- <sup>28</sup> Instituto de Física Corpuscular, IFIC, CSIC and Universidad de Valencia, Spain

Received: date / Revised version: date

**Abstract.** The double-differential production cross-section of positive pions,  $d^2\sigma_{\pi^+}/dpd\Omega$ , measured in the HARP experiment is presented. The incident particles are 8.9 GeV/c protons directed onto a beryllium target with a thickness of 5% of a nuclear interaction length. The measured cross-section has a direct impact on the prediction of neutrino fluxes for the MiniBooNE and SciBooNE experiments at Fermilab. After cuts, 13 million protons on target produced about 96,000 reconstructed secondary tracks which were used in this analysis. Cross-section results are presented in the kinematic range  $0.75 \text{ GeV}/c \leq p_{\pi} \leq 6.5 \text{ GeV}/c$  and  $30 \text{ mrad} \leq \theta_{\pi} \leq 210 \text{ mrad}$  in the laboratory frame.

**PACS.** PACS-key describing text of that key – PACS-key describing text of that key

## 1 Introduction

The HARP experiment was designed to make measurements of hadron yields from a large range of nuclear targets and for incident particle momenta from 1.5 GeV/c – 15 GeV/c. Among its primary goals were to contribute to the detailed understanding of neutrino beams of several experiments, including:

- The K2K experiment, which has recently published its final results [2] confirming the evidence of atmospheric oscillations observed by Super-Kamiokande [3].
- The MiniBooNE experiment [4], which recently excluded [5] two neutrino appearance-only oscillations as an explanation of the LSND anomaly [6], in the hypothesis that the oscillations of neutrinos and antineutrinos are the same. The MiniBooNE detector will also be used to measure neutrino interaction cross-sections for which an absolute prediction of neutrino fluxes becomes of particular importance.
- The SciBooNE experiment [9], which will take data in the same neutrino beam used by MiniBooNE in order to perform a precision measurement of neutrino cross-sections in the energy region around 1 GeV.

The calculation of the flux and relative neutrino composition of a neutrino beam requires a precise measurement of the interaction cross-section between the beam particles and the target material. In the case of the K2K and the MiniBooNE and SciBooNE experiments, the dominant component of the beam (muon neutrinos) comes from the decay of positive pions produced in the collisions of incident protons on a nuclear target.

<sup>a</sup> Now at FNAL, Batavia, Illinois, USA.

<sup>b</sup> Jointly appointed by Nuclear and Astrophysics Laboratory, University of Oxford, UK.

<sup>c</sup> Now at Codian Ltd., Langley, Slough, UK.

<sup>d</sup> Now at University of Glasgow, UK.

<sup>e</sup> Also supported by LPNHE, Universités de Paris VI et VII, Paris, France.

<sup>f</sup> Supported by the CERN Doctoral Student Programme.

<sup>g</sup> Now at Imperial College, University of London, UK.

<sup>h</sup> ITEP, Moscow, Russian Federation.

<sup>i</sup> Permanently at Instituto de Física de Cantabria, Univ. de Cantabria, Santander, Spain.

<sup>j</sup> Now at SpinX Technologies, Geneva, Switzerland.

<sup>k</sup> Now at TRIUMF, Vancouver, Canada.

<sup>l</sup> Now at University of St. Gallen, Switzerland.

<sup>m</sup> On leave of absence from Ecoanalitica, Moscow State University, Moscow, Russia.

<sup>n</sup> Now at Çukurova University, Adana, Turkey.

<sup>o</sup> Now at III Phys. Inst. B, RWTH Aachen, Aachen, Germany.

<sup>p</sup> On leave of absence from INFN, Sezione di Ferrara, Italy.

<sup>q</sup> Now at CERN, Geneva, Switzerland.

<sup>r</sup> Now at University of Rome Tor Vergata, Italy.

<sup>s</sup> Now at Lawrence Berkeley National Laboratory, Berkeley, California, USA.

<sup>t</sup> K2K Collaboration.

<sup>u</sup> MiniBooNE Collaboration.

<sup>v</sup> Now at Section de Physique, Université de Genève, Switzerland, Switzerland.

<sup>w</sup> Now at Royal Holloway, University of London, UK.

<sup>x</sup> Now at University of Sussex, Brighton, UK.

<sup>y</sup> Now at ESA/ESTEC, Noordwijk, The Netherlands.

To compute the  $\nu_\mu$  flux one needs a  $4\pi$  parameterization of the differential cross section,  $d^2\sigma^{\pi^+}/dpd\Omega$ , which, in order to be reliable, must be based on a wide-acceptance, precise measurement. The physics program of the HARP experiment includes the measurement of these cross-sections.

An earlier publication reported measurements of the  $\pi^+$  cross-sections from an aluminum target at 12.9 GeV/c [10]. This corresponds to the energies of the KEK PS and the target material used by the K2K experiment. The K2K oscillation result relies on both the measurement of an overall deficit of muon neutrino interactions and on the measurement of an energy spectrum deformation observed at the Super-Kamiokande far detector compared to the no-oscillations expectations. Introducing the HARP experimental input in the K2K oscillation analysis has been particularly beneficial in reducing the systematic uncertainty in the overall number of muon neutrino interactions expected; the near-to-far flux extrapolation contribution to this uncertainty was reduced from 5.1% [1] to 2.9% [2].

Our next goal is to contribute to the understanding of the MiniBooNE and SciBooNE neutrino fluxes. They are both produced by the Booster Neutrino Beam at Fermilab which originates from protons accelerated to 8.9 GeV/c by the Fermilab Booster before being collided against a beryllium target. As was the case for the K2K beam, an important input for the calculation of the resulting  $\nu_\mu$  flux is the  $\pi^+$  production cross-sections from a beryllium target at 8.9 GeV/c, which will be presented in this paper.

The HARP experimental apparatus is effectively divided into two tracking and particle identification sub-systems, a small-angle/high-momentum detection system ( $\theta$ : 0–0.25 rad,  $p$ : 0.5–8 GeV/c) and a large-angle/low-momentum system ( $\theta$ : 0.35–2.15 rad,  $p$ : 0.1–0.8 GeV/c). Fig. 1 shows a schematic of the HARP detector. Five modules of the NOMAD drift chambers [8] (NDC1-5) and the dipole magnet comprise the forward spectrometer; a time-of-flight wall (TOFW), Cherenkov detector (CHE) and electromagnetic calorimeter (ECAL) make up the particle identification (PID) system. The large angle tracking and PID system is comprised of a time projection chamber (TPC) and resistive plate chambers (RPCs). The relevant meson production for the creation of the MiniBooNE and SciBooNE neutrino fluxes is forward (0–0.30 rad) and at large momenta (0.5–6 GeV/c). These ranges are best covered by the forward tracking system and PID detectors and so the large angle system is not used in the present analysis.

The results reported here are based on data taken in 2002 in the T9 beam of the CERN PS. About 2.3 million incoming protons were selected. After cuts, 95,897 reconstructed secondary tracks were used in the analysis. The absolute normalization of the cross-section was determined using 204,295 ‘minimum-bias’ trigger events.

The analysis used in the calculation of the p-Be  $\pi^+$  production cross-sections being presented here follows largely from that used in a previous publication of p-Al  $\pi^+$  production cross-sections [10]. The present analysis description, therefore, will focus on the *differences* in the analysis compared to the p-Al publication.

This paper is organized as follows. In Section 2 we summarize the main changes made to the analysis since the p-Al

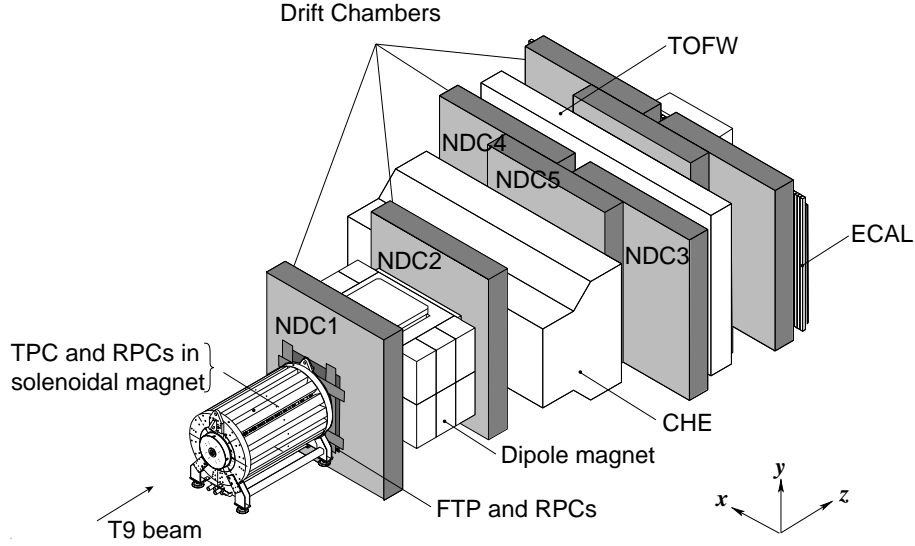


**Fig. 1.** Schematic layout of the HARP spectrometer. The convention for the coordinate system is shown in the lower-right corner. The three most downstream (unlabeled) drift chamber modules are only partly equipped with electronics and not used for tracking.

publication. In Section 3 we describe the calculation of the cross-section and define its components. The following three sections expand on aspects of the analysis where significant changes have been made since the previous publication. Section 4 describes event and track selection and reconstruction efficiencies. Section 5 discusses the determination of the momentum resolution and scale in the forward spectrometer. Section 6 summarizes the particle identification techniques. Physics results are presented in Section 7. Section 8 discusses the relevance of these results to neutrino experiments. Finally, a summary is presented in Section 9.

## 2 Summary of analysis changes since the HARP p-Al publication

The analyses of the 12.9 GeV/c p-Al data and the 8.9 GeV/c p-Be data are largely the same. To avoid repetition of information, the reader is referred to that earlier publication for many details not directly discussed in the present paper. The sections concerning the experimental apparatus, the description of the tracking algorithm for the forward spectrometer and the method of calculating the track reconstruction efficiency are all directly valid here. The method of particle identification has not changed; it is only the PID detector hit selections and therefore their response functions which have been significantly improved. The most important improvements introduced in this analysis compared with the one presented in [10] are:

- An improvement in the  $\chi^2$  minimization performed as part of the tracking algorithm has eliminated the anomalous dip in tracking efficiency above 4 GeV/c shown in [10]. The tracking efficiency is now  $\geq 97\%$  everywhere above 2 GeV/c. (See Sec. 4.3).
- Studies of HARP data other than that described here have enabled a validation of our Monte Carlo simulation of low-energy hadronic interactions in carbon. Specifically, we have

compared low energy p+C and  $\pi$ +C cross-sections to distributions from the Binary cascade [13] and Bertini intra-nuclear cascade [14] hadronic interaction models used to simulate the secondary interactions of p, n and  $\pi^\pm$ . The material in the HARP forward spectrometer where tertiary tracks might be produced is predominantly carbon. Consequently, the systematic error on the subtraction of tertiary tracks has been reduced from 100% in [10] to 50%. (See Sec. 4.4).

- Analysis techniques were developed for comparing the momentum reconstructions in data and Monte Carlo allowing data to be used to fine-tune the drift chamber simulation parameters. These efforts have reduced the momentum scale uncertainty from 5% in [10] to 2% in the present analysis and provided a better understanding of the momentum smearing caused by the HARP spectrometer, including our knowledge of the non-Gaussian contributions to the resolution function. (See Sec. 5).
- New selection cuts for PID hits in TOFW and in CHE have resulted in much reduced backgrounds and negligible efficiency losses. Consequently, the uncertainty on the cross-section arising from particle identification was reduced by a factor of seven to 0.5% making PID now a negligible contribution to the systematic error in pion yield measurements at forward angles. (See Sec. 6).
- Improved knowledge of the proton beam targeting efficiency and of fully correlated contributions to track reconstruction and particle identification efficiencies have reduced the overall normalization uncertainty on the pion cross-section measurement from 4% to 2%.
- Significant increases in Monte Carlo production have reduced uncertainties from Monte Carlo statistics and allowed studies to reduce certain systematics to be made.

The statistical precision of the data, however, is noticeably worse. The 8.9 GeV/c beryllium and empty-target data sets are both smaller than the corresponding 12.9 GeV/c sets, with

73% and 42% of the protons-on-target for the target and empty-target configurations, respectively. The statistics of the target sample is further reduced by the p-Be total interaction cross-section being roughly 50% of the p-Al total cross-section.

In the present paper the p-Be cross-sections are presented in 13 momentum bins from 0.75 GeV/c– 6.5 GeV/c whereas the p-Al cross-sections were presented in 8 bins. This new binning was selected to attain roughly equal statistical and systematic uncertainties - on average 6.3% statistical and 7.4% systematic in the 78  $(p, \theta)$  bins - while maximizing the amount of spectral information provided by the measurement. It should be noted that the magnitude of fractional systematic errors arising from the momentum resolution and scale will be affected by the fineness of the binning. In particular, in the present paper, the momentum scale uncertainty has been reduced from 5% to 2% since the p-Al publication yet this does not lead to a smaller systematic contribution on the measured cross-section. This is expected since, simultaneous to the improved reconstruction, most momentum bins have been narrowed by a factor of 2.

In the end, the statistical plus systematic uncertainty on the total integrated cross-section has improved from 5.8% in p-Al to 4.9% in p-Be. Due to rebinning and larger statistical errors, the average bin-to-bin uncertainty on the differential cross-section has changed from 8.2% in p-Al to 9.8% in p-Be.

We point out that a re-analysis of the proton-aluminum data incorporating these changes yields results consistent with those published in [10] within the systematic errors reported there.

### 3 Calculation of the double-differential inelastic cross-section

The goal of this analysis is to measure the inclusive yield of positive pions from proton-beryllium collisions at 8.9 GeV/c:

$$p + \text{Be} \rightarrow \pi^+ + X$$

The absolutely normalized double-differential cross-section for this process can be expressed in bins of pion kinematic variables in the laboratory frame,  $(p_\pi, \theta_\pi)$ , as

$$\frac{d^2\sigma^{\pi^+}}{dpd\Omega}(p_\pi, \theta_\pi) = \frac{A}{N_A \cdot \rho \cdot t} \cdot \frac{1}{\Delta p \Delta \Omega} \cdot \frac{1}{N_{\text{pot}}} \cdot N^{\pi^+}(p_\pi, \theta_\pi), \quad (1)$$

where:

- $\frac{d^2\sigma^{\pi^+}}{dpd\Omega}$  is the cross-section in  $\text{cm}^2/(\text{GeV}/c)/\text{sr}$  for each  $(p_\pi, \theta_\pi)$  bin covered in the analysis
- $\frac{A}{N_A \cdot \rho}$  is the reciprocal of the number density of target nuclei for beryllium ( $1.2349 \cdot 10^{23}$  per  $\text{cm}^3$ ).  $A$  is the atomic mass of beryllium,  $N_A$  is Avogadro's number and  $\rho$  is the density of beryllium.
- $t$  is the thickness of the beryllium target along the beam direction. The target has a cylindrical shape, with a measured thickness and diameter of  $t = (2.046 \pm 0.002)$  cm and  $d \simeq 3.0$  cm, respectively.
- $\Delta p$  and  $\Delta \Omega$  are the bin sizes in momentum and solid angle, respectively.<sup>1</sup>

<sup>1</sup>  $\Delta p = p_{\text{max}} - p_{\text{min}}$ ;  $\Delta \Omega = 2\pi(\cos(\theta_{\text{min}}) - \cos(\theta_{\text{max}}))$

- $N_{\text{pot}}$  is the number of protons on target after event selection cuts (see section 4.1).
- $N^{\pi^+}(p_\pi, \theta_\pi)$  is the yield of positive pions in bins of momentum and polar angle in the laboratory frame.

The true pion yield,  $N^{\pi^+}(p_\pi, \theta_\pi)$ , is related to the measured one,  $N^{\pi^+}(p'_\pi, \theta'_\pi)$ , by a set of efficiency corrections and kinematic smearing matrices. In addition, there is a small but non-negligible mis-identification of particle types, predominantly between pions and protons. Therefore, both yields must be measured simultaneously in order to correct for migrations. Eq. 1 can be generalized to give the inclusive cross-section for a particle of type  $\alpha$

$$\frac{d^2\sigma^\alpha}{dpd\Omega}(p, \theta) = \frac{A}{N_A \cdot \rho \cdot t} \cdot \frac{1}{\Delta p \Delta \Omega} \cdot \frac{1}{N_{\text{pot}}} \cdot M_{p\theta\alpha p'\theta'\alpha'}^{-1} \cdot N^{\alpha'}(p', \theta'), \quad (2)$$

where reconstructed quantities are marked with a prime and  $M_{p\theta\alpha p'\theta'\alpha'}^{-1}$  is the inverse of a matrix which fully describes the migrations between bins of generated and reconstructed quantities, namely: laboratory frame momentum,  $p$ , laboratory frame angle,  $\theta$ , and particle type,  $\alpha$ . In practice, the matrix  $M$  can be factorized into a set of individual corrections, as will be done here. The reasons for doing this are threefold:

- Not all efficiencies and migrations are functions of all three variables. Particle identification efficiencies and migrations do not depend on the angle,  $\theta$ , and the tracking efficiency and momentum resolution are the same for pions and protons.
- Using techniques described below the tracking efficiency and particle identification efficiency and migrations can be determined from the data themselves and do not rely on simulation. This is, of course, preferable wherever possible.
- Measuring and applying the corrections separately will ease the assessment of systematic errors as will be discussed in Section 7.

The form of the corrections can be separated into two basic categories: absolute efficiencies and bin-to-bin migrations between true and reconstructed quantities. In particular, migrations in momentum and in particle identification are carefully considered. The various efficiency corrections can, therefore, be functions of either reconstructed quantities or true ones, and must then be applied at the appropriate point in the analysis. This is important given that some corrections, as mentioned above, are measured from the data themselves where one has only reconstructed quantities.

Further, we are interested only in *secondary*  $\pi^+$  created in *primary* interactions of beam protons with beryllium nuclei. Pions created in interactions other than p+Be at 8.9 GeV/c are a background to the measurement. *Tertiary* particles are those created when secondary particles decay or inelastically interact downstream of the target in air or detector materials and are not to be included in the measured cross-section.

In the present analysis,  $M_{p\theta\alpha p'\theta'\alpha'}^{-1}$  has been factorized into the following components. Note that  $\theta_x = \tan^{-1}(p_x/p_z)$  and  $\theta_y = \tan^{-1}(p_y/p_z)$  are useful variables for viewing the de-

tector in  $x, y$ -plane coordinates and are related to the standard polar angle by  $\theta = \tan^{-1}(\sqrt{\tan^2 \theta_x + \tan^2 \theta_y})$ .

- $\varepsilon^{\text{recon}}(p', \theta'_x, \theta'_y)$  is the efficiency for the reconstruction of an ‘analysis track’. An ‘analysis track’ is defined to include a momentum measurement as well as a matched time-of-flight hit needed for particle identification such that  $\varepsilon^{\text{recon}} = \varepsilon_{\text{track}} \cdot \varepsilon_{\text{TOFW-match}}$ .
- $\varepsilon^{\text{acc}}(\theta)$  is the correction for the geometric acceptance of the spectrometer and is a purely analytical function based on the assumption of azimuthal symmetry in hadron production and the fiducial cuts used in the analysis. See [10] for a full description of the acceptance correction and its dependence on the  $\theta_y$  fiducial volume cut.
- $M_{pp'}^{-1}(\theta')$  is the matrix describing the migration between bins of measured and generated momentum. There is a unique matrix for each angular bin in the analysis since the momentum resolution and bias vary with angle.
- $M_{\theta\theta'}^{-1}(p)$  is a unit matrix, implying that angular migrations, which are small, are being neglected.
- $\eta^{\text{absorb}}(p, \theta_x, \theta_y, \alpha)$  is the absorption plus decay rate of secondary particles before reaching the time-of-flight wall which is required for particle identification.
- $(1 - \eta^{\text{tert}}(p', \theta'_x, \theta'_y, \alpha))$  corrects for the fraction,  $\eta^{\text{tert}} = \frac{N^{\text{rec-tert}}}{N^{\text{rec}}}$ , of total tracks passing reconstruction cuts,  $N^{\text{rec}}$ , which are actually tertiary particles,  $N^{\text{rec-tert}}$ .
- $\varepsilon^{\text{e-veto}}(p, \alpha)$  is the efficiency for particles of type  $\alpha$  passing the electron veto cut used to remove electrons from the analysis track sample as described below.
- $M_{\alpha\alpha'}^{-1}(p)$  is the particle identification efficiency and migration matrix, assumed uniform in  $\theta$ .

Once again primed variables are those measured and unprimed variables are the true quantities (i.e. after unsmearing). Expanding  $M_{p\theta\alpha p'\theta'\alpha'}^{-1}$  into these individual corrections and taking care of the order in which they are applied gives us the final equation for calculating the absolute cross-section from the measured yields.

$$\begin{aligned} \frac{d^2\sigma^\alpha}{dpd\Omega}(p, \theta) &= \frac{A}{N_A \cdot \rho \cdot t} \cdot \frac{1}{\Delta p \Delta \Omega} \cdot \frac{1}{N_{\text{pot}}} \\ &\times M_{\alpha\alpha'}^{-1}(p) \cdot \frac{1}{\varepsilon^{\text{e-veto}}(p, \alpha)} \\ &\cdot \frac{1}{1 - \eta^{\text{absorb}}(p, \theta_x, \theta_y, \alpha)} \\ &\cdot M_{pp'}^{-1}(\theta') \cdot (1 - \eta^{\text{tert}}(p', \theta'_x, \theta'_y, \alpha)) \\ &\cdot \frac{1}{\varepsilon^{\text{acc}}(\theta')} \cdot \frac{1}{\varepsilon^{\text{recon}}(p', \theta'_x, \theta'_y)} \\ &\cdot N^{\alpha'}(p', \theta'). \end{aligned} \quad (3)$$

There are two additional aspects of the analysis methods which are worth mentioning. First, particle distributions are built by multiplying a set of correction weights for each reconstructed track and weighting events before they are added to the total yields. In this way a single reconstructed track is ‘spread’ over multiple true momentum bins according to the elements of

$M_{pp'}^{-1}(\theta')$ , and the population in each true bin is comprised of tracks from all reconstructed momentum bins. This approach avoids the difficulties associated with inverting a large smearing matrix due to potential singularity of the matrix as well as potential pathologies in the inverted matrix caused by a loss of information at the kinematic boundaries of the matrix itself. The drawback to this method is that one has some sensitivity to the underlying spectrum in the Monte Carlo used to generate the matrix (see Sec. 5).

Second, there is a background associated with beam protons interacting in materials other than the nuclear target (parts of the detector, air, etc.). These events can be subtracted by using data collected without the nuclear target in place. We refer to this as the ‘empty target subtraction’:

$$N^{\alpha'}(p', \theta') \rightarrow [N_{\text{target}}^{\alpha'}(p', \theta') - N_{\text{empty}}^{\alpha'}(p', \theta')].$$

The final form of the cross-section calculation is then given by making the above substitution into Eq. 3.

## 4 Track selection and reconstruction efficiency corrections

### 4.1 Event selection

Protons are identified in the T9 beam at 8.9 GeV/c exactly as in the 12.9 GeV/c data set and as described in reference [10]. Two threshold Cherenkov detectors (BCA and BCB) placed in the beam line are used to select protons by requiring a value consistent with the pedestal in both detectors. The beam Cherenkov pulse height distributions for the 8.9 GeV/c beam are shown in Fig. 2. Protons were selected by requiring a pulse height less than 120 counts in both detectors, and Fig. 3 shows the time-of-flight distributions of those beam tracks identified as protons and pions by the Cherenkov selection. The beam time-of-flight system is made of two identical scintillator hodoscopes, TOFA and TOFB, recuperated from the previous NA52 experiment and a small target-defining trigger counter (TDS). TOFA-TOFB and TOFA-TDS measure time differences over a distance of 21.4 m and 24.3 m, respectively. We see in Fig. 3 that the two time peaks are consistent with the proton and pion hypotheses at 8.9 GeV/c.

Only events with a single reconstructed beam track in the four beam multi-wire proportional chambers (MWPCs) and no signal in the beam halo counters are accepted. This MWPC track is used to determine the impact position and angle of the beam particle on the target. A time measurement in one of three beam timing detectors consistent with a beam particle is also required for determining the arrival time of the proton at the target,  $t_0$ . This  $t_0$  is necessary for calculating the time-of-flight of secondary particles.

The full set of criteria for selecting beam protons for this analysis is as follows:

- ADC count less than 120 in both beam Cherenkov A and beam Cherenkov B

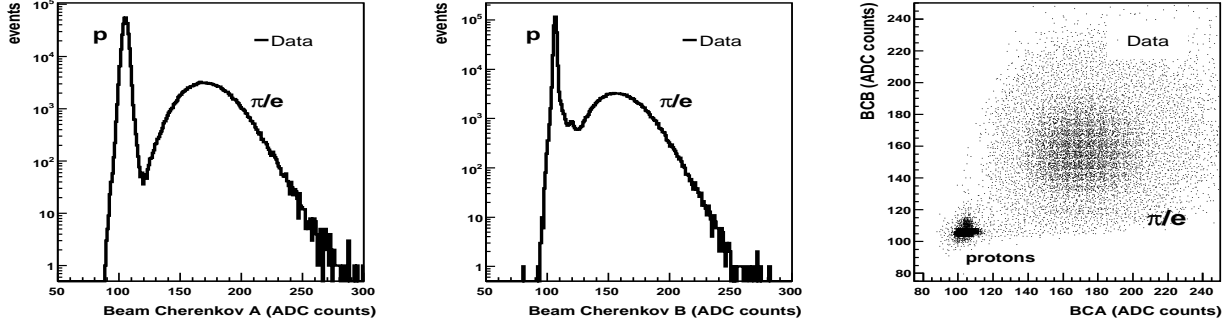


**Fig. 2.** Beam Cherenkov pulse height distributions. BCA in the left panel, BCB in the middle, and BCB vs. BCA in the right panel. The electron and pion tagging efficiency is found to be close to 100%; the peaks are separated by  $\approx 3\sigma$  in both detectors. By requiring a value compatible with a pedestal in both Cherenkov detectors the beam protons are clearly separable from pions and electrons as seen in the right panel.

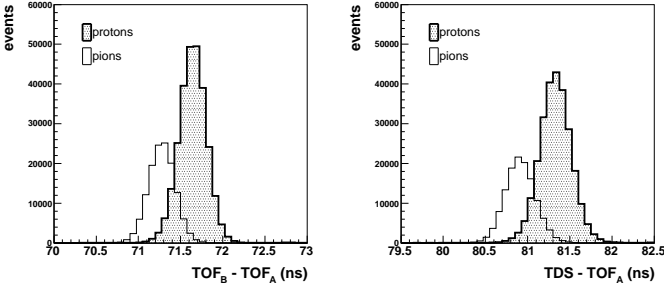


**Fig. 3.** Beam time-of-flight distributions. The time difference between TOFA and TOFB is shown in the left panel. The right panel is the time difference between TOFA and the TDS. The shaded distributions are for particles identified as protons by the Cherenkov detectors as described in the text. The open histograms are all other beam tracks: pions, electrons and muons from pion decays.

- time measurement(s) in TOFA, TOFB and/or TDS which are needed for calculating the arrival time of the beam proton at the target,  $t_0$
- extrapolated position at the target within a 10 mm radius of the center of the target
- extrapolated angle at the target less than 5 mrad
- no signal in the beam halo counters

Prior to the above cuts, for data taken with a nuclear target, a downstream trigger in the forward trigger plane (FTP) was required to record the event.<sup>2</sup> The FTP is a double plane of scintillation counters covering the full aperture of the spectrometer magnet except a 60 mm central hole for allowing non-interacting beam particles to pass. The efficiency of the FTP is measured to be  $>99.8\%$ .

Using the FTP as an interaction trigger necessitates an additional set of unbiased, pre-scaled triggers for absolute normalization of the cross-section. Beam protons in the pre-scale

<sup>2</sup> empty target data sets are recorded with an unbiased trigger setting since these samples are used to calibrate the experimental apparatus and not just in the empty target subtraction for cross-section measurements.

trigger sample (1/64 of the total trigger rate for the 8.9 GeV/c Be data set) are subject to exactly the same selection criteria as FTP trigger events allowing the efficiencies of the selections to cancel and adding no additional systematic uncertainty to the absolute normalization of the result. These unbiased events are used to determine the  $N_{\text{pot}}$  used in the cross-section formula and listed in Table 4.2. The number of protons-on-target is known to better than 1%.

Applying these criteria we are left with the event totals summarized in Table 4.2.

## 4.2 Secondary track selection

The following criteria have been applied to select tracks in the forward spectrometer for the accepted events:

- a successful momentum reconstruction using downstream track segments in NDC modules 2, 3, 4 or 5 and the position of the beam particle at the target as an upstream constraint (here, *upstream* and *downstream* are relative to the spectrometer magnet);
- a reconstructed vertex radius (*i.e.* the distance of the reconstructed track from the  $z$ -axis in a plane perpendicular to this axis at  $z = 0$ )  $r \leq 200$  mm;
- number of hits in the road around the track in NDC1  $\geq 4$  and average  $\chi^2$  for these hits with respect to the track in NDC1  $\leq 30$  (this is applied to reduce non-target interaction backgrounds);
- number of hits in the road around the track in NDC2  $\geq 6$  (this is applied to reduce non-target interaction backgrounds);
- a matched TOFW hit passing the quality cuts described in Sec. 6.2.1;
- reconstructed angles are within the fiducial volume to be used for this analysis,  $-210 \text{ mrad} \leq \theta_x \leq 0 \text{ mrad}$  and  $-80 \text{ mrad} \leq \theta_y \leq 80 \text{ mrad}$ .

These cuts are identical to those used in the analysis of the p-Al data except for the reconstructed vertex radius  $\leq 200$  mm cut. It was found that due to a feature of the algorithm this additional requirement improved the momentum resolution considerably at reconstructed momenta below  $\approx 1.5$  GeV/c.

Data Set	Be 5% 8.9 GeV/c	8.9 GeV/c Empty Target
protons on target	13,074,880	1,990,400
total events processed	4,682,911	413,095
events with accepted beam proton	2,277,657	200,310
beam proton events with FTP trigger	1,518,683	91,690
total good tracks in fiducial volume	95,897	3,110

**Table 1.** Total number of events in the 8.9 GeV/c beryllium 5%  $\lambda_I$  target and empty target data sets, and the number of protons on target as calculated from the prescaled trigger count.

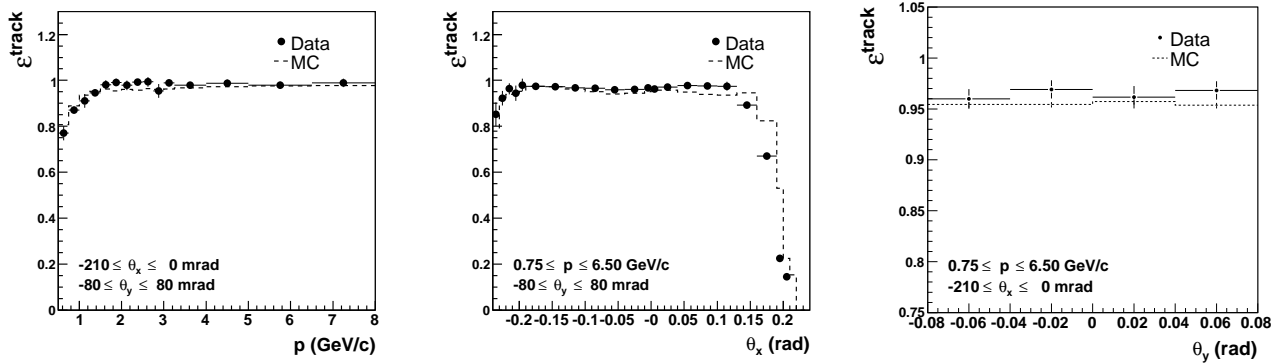


**Fig. 4.** Tracking efficiency for positive particles traversing the detector using the target as upstream track constraint as a function of particle momentum (upper left), production angle in the horizontal plane,  $\theta_x$  (upper right), and production angle in the vertical plane,  $\theta_y$  (lower). The  $\theta_y$  plane is orthogonal to the spectrometer bending plane and not sensitive to the momentum dependent acceptance, and the bottom panel shows the purest measure of the average track reconstruction efficiency within the fiducial volume to be 96%–97%.

Applying these cuts to reconstructed tracks in accepted events we are left with 95,897 total good tracks in the beryllium thin target data set as listed in Table 4.2.

### 4.3 Track reconstruction efficiency

The track reconstruction efficiency has been measured from the data exactly as described in [10]. The efficiency is shown in Fig. 4. The effects of the two changes in track reconstruction are evident in the efficiency curves. First, the efficiency is now flat and  $\approx 97\%$  above 2 GeV/c due to the improvement in the  $\chi^2$  minimization done as part of the tracking algorithm. Second, the loss of efficiency at momenta below 1.5 GeV/c is due to the reconstructed vertex radius  $\leq 200$  mm cut discussed above. But, as before, the tracking efficiency can be measured from the data themselves, so the systematic error on the correction comes only from the statistical uncertainty in the sample used to calculate the correction. As in the p-Al publication, the 12.9 GeV/c aluminum data and the 8.9 GeV/c beryllium data have been combined to minimize this uncertainty. The drop in efficiency at large, positive values of  $\theta_x$  is due to geometric acceptance as low momentum tracks are bent out of the spectrometer missing the downstream chambers. The present analysis is performed using tracks in the range  $-0.210 \text{ rad} \leq \theta_x \leq 0 \text{ rad}$  where the acceptance is flat in momentum.

### 4.4 Absorption, decay and tertiary track corrections

The correction for absorption and decay refers to secondary particles created in the nuclear target that never make it to the time-of-flight wall for detection and possible identification. Figure 1 shows the location of the time-of-flight scintillator wall just beyond the back plane of drift chamber modules NDC3, NDC4 and NDC5. We use the Monte Carlo simulation to determine the size of the correction and the result is shown in Fig. 5. Note this is an upward adjustment to the raw yield measured and is implemented as  $1/(1 - \eta^{absorb}(p, \theta_x, \theta_y, \alpha))$  in Eq. 3. The absorption correction (which includes pion decays) is a function of  $\theta_x$  and  $\theta_y$  because it depends on the amount and type of physical material a particle passes through, thus the geometry of the detector. It is a function of  $\alpha$  because of the different interaction cross-sections and possible decay rates of hadrons. This correction is separated from the tertiary correction discussed below because it does not depend on event multiplicity, kinematics or other details of the hadron production model used in the simulation, but only the total interaction cross-sections which are significantly more certain. In fact, the relevant cross-sections are typically known to  $\approx 10\%$  and we assume this uncertainty on the absorption correction just as in the p-Al publication. Because the correction is of order 30–40% for pions, the average systematic error contribution to the cross-section turns out to be 3.6%.

The tertiary correction refers to the subtraction of reconstructed tracks which are actually reconstructions of tertiary particles, *i.e.* particles produced in inelastic interactions or de-

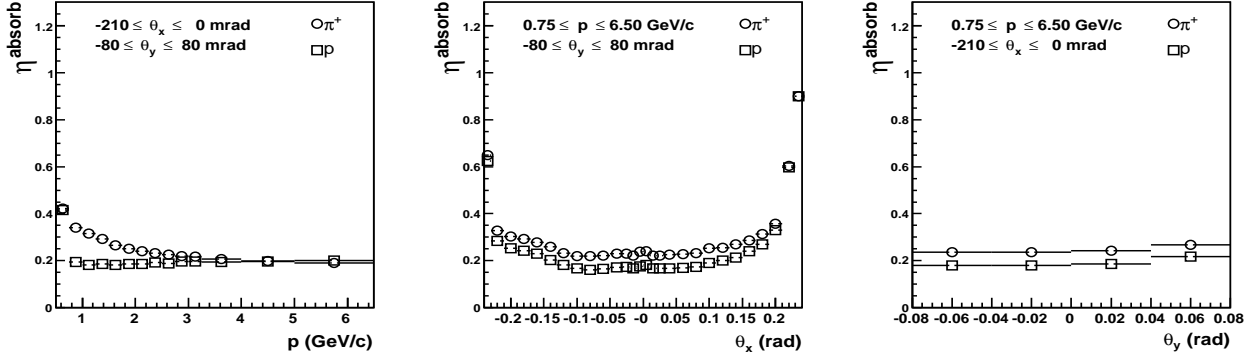


**Fig. 5.** Absorption corrections for pions and protons according to Monte Carlo simulation as a function of particle momentum (left), production angle in the horizontal plane,  $\theta_x$  (center) and production angle in the vertical plane,  $\theta_y$  (right).

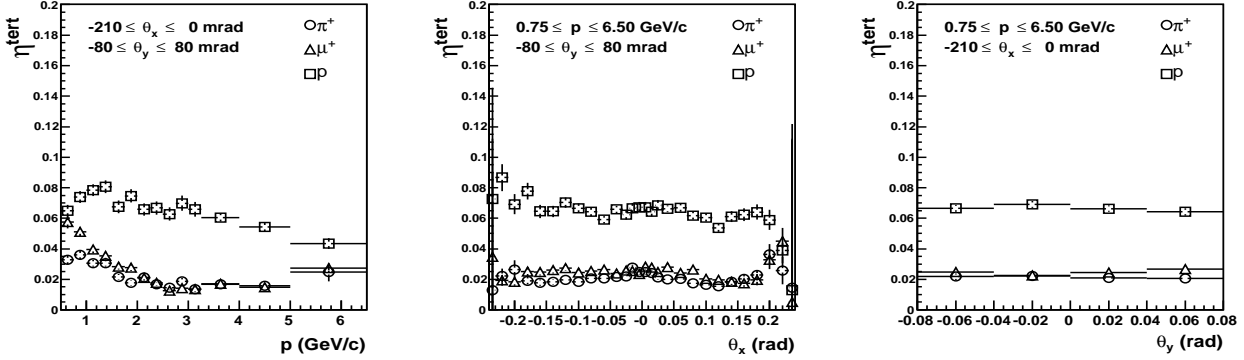


**Fig. 6.** Tertiary particle rates for pions, muons (which get identified as pions) and protons according to Monte Carlo simulation as a function of particle momentum (left), production angle in the horizontal plane,  $\theta_x$  (center) and production angle in the vertical plane,  $\theta_y$  (right).

cays of true secondary particles and not in primary interactions of 8.9 GeV/c protons with beryllium nuclei (See section 3). The tertiary subtraction includes muons created in decays which are falsely identified as pions nearly 100% of the time due to their high  $\beta$ . The correction is significantly smaller than the absorption correction (compare Figs. 5 and 6), but is less certain, so the contribution to the systematic error is non-negligible. This tertiary subtraction is also generated using the Monte Carlo simulation but is dependent on the details of the hadron production model used in the simulation. Most of the material where tertiary particles might be produced in the detector is carbon, so it is the simulation of inelastic interactions of low-energy protons and pions in carbon that become important in generating this correction. Previously this correction was assumed to be 100% uncertain, but comparisons of low momentum HARP  $p+C$ ,  $\pi^+ + C$  and  $\pi^- + C$  data to the hadronic models used in the simulation have verified these models to  $\approx 50\%$  and allowed us to lower the systematic error on this correction. Fig. 6 shows the average size of the correction to the  $\pi^+$  yield to be about 4% ( $2\% \pi^+ + 2\% \mu^+$ ), so the average systematic error on the cross-section coming from the subtraction of tertiaries ends up being 1.8%.

## 5 Momentum resolution and scale corrections

Two important sources of systematic uncertainty are the momentum resolution and the absolute momentum scale of the reconstruction. Each, in general, vary with the value of the true momentum and angle of the track. The Monte Carlo will be used to generate corrections to the measured momenta so a validation of the simulation becomes necessary. Three techniques have been developed to compare the resolutions of reconstructed quantities in data and Monte Carlo of which only one was available at the time of the p-AI paper. The challenge is to isolate a set of tracks in the data sample with a known momentum. The three methods are described fully below but, briefly, they are based on empty target data sets, samples of elastic scattering events and using the excellent resolution of the time-of-flight system to determine the momentum. Results from these studies have been used to tune the detector simulation and to estimate a systematic uncertainty due to momentum resolution and scale.

A multiplicative momentum scale correction is applied to all reconstructed tracks in the data to remove a  $\theta_x$ ,  $\theta_y$  dependence seen in calibration samples. After this correction we see



no significant momentum mis-calibration beyond the 2% absolute momentum scale uncertainty estimated using the elastic scattering technique (see Sec. 5.2). The minimum ratio of momentum bin width over momentum bin central value is 8%, four times this value. An average uncertainty on the  $\pi^+$  cross-section of 3.6% is estimated from this effect (the effect is dependent on the steepness of the pion and proton spectra, the size of the momentum bias and the momentum binning).

The resolution of the momentum measurement leads to smearing in the reconstructed pion spectrum. Momentum ‘unsmearing’ is performed in the analysis by using the Monte Carlo to generate a momentum migration matrix,  $M_{pp'}^{-1}(\theta')$  which describes how a reconstructed momentum value is distributed across bins of true momentum. The accuracy of this migration matrix, which is generated from Monte Carlo samples, depends upon two factors – the similarity of the underlying hadron distributions to those in the data and the agreement between the resolutions of reconstructed quantities in the data and Monte Carlo relative to the true momenta. The latter, the agreement between the resolutions of reconstructed quantities in data and Monte Carlo, is the topic of the next three subsections. The techniques developed have been used to tune parameters of the simulation to achieve good agreement. The first effect, the similarity of the hadron spectra to the data, therefore, will dominate the systematic error for this correction. We estimate a momentum resolution uncertainty by performing the cross-section analysis using migration matrices generated from Monte Carlo samples which use different hadronic models. The average uncertainty on the  $\pi^+$  cross-section estimated from this effect is 3.4%.

### 5.1 Momentum calibration using empty target data sets

The first method for calibrating the momentum reconstruction uses empty target data sets where the incoming beam momentum value acts as the known momentum. Fig. 7 shows the result of such a study using empty target data and Monte Carlo samples for beam momenta of 1.5, 3.0, 5.0, 8.0, 8.9, 12.0, 12.9 and 15.0 GeV/c. The shape of the  $\sigma_p/p$  curve versus momentum is as expected, and the agreement between data and Monte Carlo is excellent. For the previous analysis [10] only these ‘test-beam data’ were available, sampling the spectrometer response on the  $z$ -axis only. Now, additional methods have been used. A method using samples of elastic scattering events extends the range to larger angles while a method employing the time-of-flight detector covers the region of low momenta. Thus the full range of relevant angles and momenta is covered.

### 5.2 Momentum calibration using elastic scattering events

The elastic scattering process provides one track in the forward direction with a momentum close to the beam momentum and a soft large angle proton. In  $p$ - $p$  and  $\pi$ - $p$  scattering the kinematics is fully determined by the measurement of the direction of one of the outgoing particles. The precision of the measurement of the angle of the forward scattered particle is

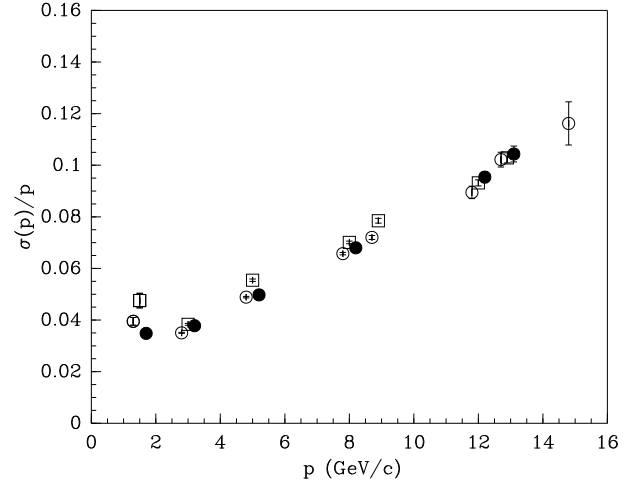


**Fig. 7.** Momentum resolution  $\sigma(p)/p$  (Gaussian fit) as a function of momentum (in GeV/c) for the drift chambers: the data were taken using several well-defined discrete beam momenta and no target for pions (open circles) and protons (open squares). Also shown (filled circles) is the corresponding resolution found using the Monte Carlo simulation.

sufficient to predict the momentum of that particle without significant error. Elastic events can be readily selected by imposing combined criteria in the large angle and forward spectrometer. The main selection is the requirement of one and only one track in the TPC, identified as a proton, and exactly one track in the forward direction. Further constraints have been used, such as a match of the kinematics of these tracks and the selection of events with exactly the expected number of hits in the trigger counters and the barrel RPC detectors around the TPC. In these selections no constraints on the momentum measurement of the forward track has been set. The purity of the selection of the elastic scattering events used in this analysis can be estimated by studying the  $p$ - $\theta$  distribution of the proton recoil tracks measured in the TPC. The two quantities are fully correlated for elastic scattering events. From the small number of events outside the expected region, one can estimate the background in the sample not to exceed 1%. The systematic error introduced by this background is negligible compared to the 2% estimated overall momentum calibration error.

Figure 8 shows the results of an analysis of elastic events using 3 GeV/c, 5 GeV/c, and 8 GeV/c beams impinging on a hydrogen target. Incoming pion and proton data are combined. The left panel reveals a momentum offset in the data of about 2% at all momenta and in three angular regions, 30 mrad–60 mrad, 60 mrad–100 mrad and 100 mrad–150 mrad. This 2% will contribute a systematic uncertainty to the final cross-section and will be discussed in Sec. 7.1. The right panel shows the RMS of the momentum measurement as a function of momentum in the same two angular regions. The resolution measured from data is compared to that in the Monte Carlo and, as with the empty target samples, the agreement is excellent.

The momentum scale and resolution measured with the elastic events extends the calibration toward larger angles than probed with the empty target data alone and make it possible to characterize the spectrometer over a larger range of its aperture.

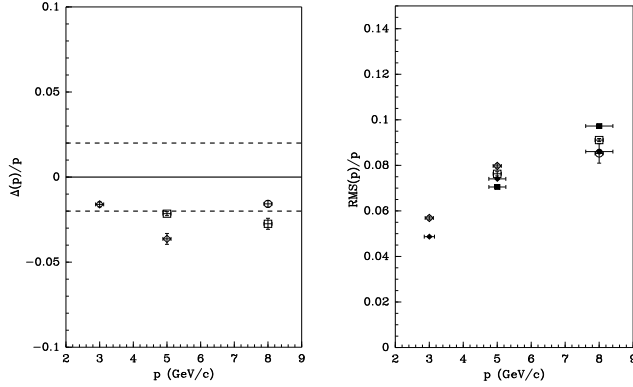


**Fig. 8.** Momentum scale  $\Delta(p)/p$  and resolution  $\sigma(p)/p$  (Gaussian fit) as a function of momentum in three angular regions (circles: 30 mrad–60 mrad; boxes: 60 mrad–100 mrad; diamonds 100 mrad–150 mrad). The data were taken using 3 GeV/c, 5 GeV/c and 8 GeV/c beams impinging on a hydrogen target. The top panel shows no significant momentum mis-calibration beyond the 2% absolute momentum scale uncertainty estimated using the elastic scattering technique. The bottom plot shows the resolutions from data (open symbols) compared with the corresponding Monte Carlo simulations (filled symbols). Incoming pion and proton data are combined.

However, the lowest momentum at which these data are available is 3 GeV/c, such that another method had to be developed to study the performance of the spectrometer for lower momentum particles.

### 5.3 Momentum calibration using time-of-flight

The TOFW system [12] can be used to provide a momentum calibration in a momentum range where the dependence of the time-of-flight on the momentum for pions is much smaller than for protons and at the same time the resolution of the TOFW is better than the prediction of  $\beta$  for protons based on the momentum measurement. For protons the sensitivity to the momentum resolution is larger than all other dependencies in the beta resolution in the region  $0.22 \text{ GeV}/c < p < 2.0 \text{ GeV}/c$ . The TOFW $\beta$  resolution is typically  $\sigma(\beta)/\beta = 0.005$ . The precision  $\sigma(\beta_{\text{pred}})/\beta$  in the calculation of  $\beta$  for protons ranges from 0.05 at 0.22 GeV/c to 0.005 at 2 GeV/c due to the momentum resolution which is of the order of 100 MeV/c in this range. Therefore the width of the  $\beta$  peak for a sample of protons selected in a small range in *measured momentum* shows a large sensitivity to the momentum resolution.

To exploit this feature for the determination of the momentum resolution at small momenta the time-response of the TOFW has to be measured for pions and protons separately. First a very clean sample of pions is selected. Particles of negative charge are selected for this purpose to provide negative pions. In principle, this sample can be contaminated by electrons and negative kaons. Antiprotons are expected to be negligible. At a momentum below the Cherenkov threshold for pions, electrons are rejected by retaining only particles without a signal in the Cherenkov detector. The remaining sample contains mainly  $\pi^-$  with a small background of  $K^-$ . This kaon background is visible in the TOF spectrum and has been taken into account.

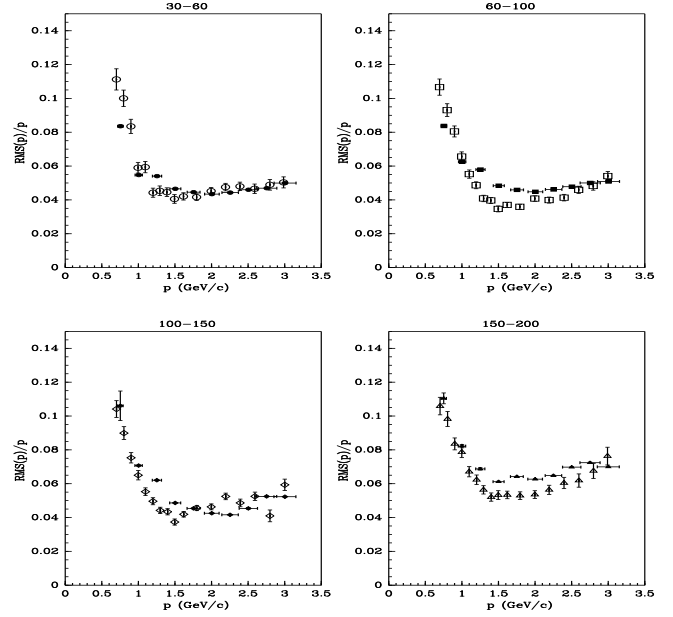


**Fig. 9.** RMS momentum resolution as a function of momentum in four angular bins (circles: 30 mrad–60 mrad; boxes: 60 mrad–100 mrad; diamonds: 100 mrad–150 mrad; triangles: 150 mrad–200 mrad). Data are shown with open symbols; Monte Carlo with filled symbols.

At a momentum above the pion Cherenkov threshold, the  $\pi^-$  sample is selected by requiring a signal in the Cherenkov. Although the electron background is expected to be small at these momenta, a selection with the calorimeter is used to reject them. The same selection is also used at momenta below Cherenkov threshold in addition to the rejection with the Cherenkov detector. Thus a sufficiently clean sample of negative pions can be obtained in the whole momentum range.

From the sample of positive particles, positrons are removed by the selection using the electron identifier. Below Cherenkov threshold only particles without signal in the Cherenkov are used. This selection retains protons, kaons and pions below pion Cherenkov threshold and only protons and kaons above the threshold. The precision of the TOFW is sufficient to provide a good separation of pions and protons below pion Cherenkov threshold. Thus, in the whole range relevant for the experiment a clean sample of protons can be obtained, albeit with a small contamination of kaons. As mentioned above, the measurement with the negative pions characterizes the TOFW response, both its absolute time and its time resolution. The negative pions also provide a perfect prediction for the behavior of the TOFW measurement for the positive pions.

The measurement of the properties of the momentum determination in the spectrometer is then obtained by selecting small regions (bins) of measured momentum and fitting the  $\beta$  spectrum of protons with a function which takes into account the width of the momentum bin, the calibrated  $\beta$  resolution and as a free parameter the momentum resolution. The results for data and Monte Carlo and in four angular regions are shown in Fig. 9. The resolution measured should be interpreted as an RMS of the momentum resolution and is larger than the  $\sigma$  of

the Gaussians fitted to the direct beam data using the runs without target, but consistent with the RMS of the latter.

Combining information from these three techniques one is able to map out the momentum resolution and scale in both data and Monte Carlo for comparison. The results indicate good agreement across a range of momenta and angles allowing us to utilize the Monte Carlo simulation to generate the momentum resolution correction matrix,  $M_{pp}^{-1}(\theta')$ .

## 6 Particle identification

The particle identification method used here follows exactly that used in the analysis of the p-Al data [10]. However, a significant improvement in efficiency and purity of the PID and, consequently, a large reduction in the systematic uncertainties on the cross-section have been realized by improving the association of PID detector hits with reconstructed tracks. We include here a description of the PID method for completeness and clarity and a full explanation of how detector hits are selected follows in the next section.

### 6.1 The pion-proton PID estimators and PID efficiency calculation

The analysis uses particle identification information from the time-of-flight and Cherenkov PID systems; the discrimination power of time-of-flight below 3 GeV/c and the Cherenkov detector above 3 GeV/c are combined to provide powerful separation of pions and protons. The calorimeter is presently used only for separating pions and electrons when characterizing the response of the other detectors. The resulting efficiency and purity of pion identification in the analysis region is excellent.

Particle identification is performed by determining the probability that a given track is a pion or a proton based on the expected response of the detectors to each particle type and the measured response for the track. Information from both detectors is combined for maximum discrimination power using a Bayesian technique,

$$P(\alpha|\beta, N_{pe}, p, \theta) = \frac{P(\beta, N_{pe}|\alpha, p, \theta) \cdot P(\alpha|p, \theta)}{\sum_{i=\pi, p, \dots} P(\beta, N_{pe}|i, p, \theta) \cdot P(i|p, \theta)} \quad (4)$$

where  $P(\alpha|\beta, N_{pe}, p, \theta)$  is the probability that a track with reconstructed velocity  $\beta$ , number of associated photo-electrons  $N_{pe}$ , and momentum and angle  $p$  and  $\theta$  is a particle of type  $\alpha$ .  $P(i|p, \theta)$  is the so-called prior probability for each particle type,  $i$ , and is a function of  $p$  and  $\theta$ . In the Bayesian approach, the priors represent one's knowledge of the relative particle populations before performing a measurement. Finally,  $P(\beta, N_{pe}|i, p, \theta)$  is the expected response ( $\beta$  and  $N_{pe}$ ) of the PID detectors for a particle of type  $i$  and momentum and angle  $p, \theta$ .

The following simplifications are applied to Eq. 4. First, we will assume no a priori knowledge of the underlying pion/proton

spectra; that is, the prior distributions will be flat and equal everywhere,  $P(i|p, \theta) = 1$  for all  $p, \theta$ . This allows the priors to be dropped from the expression, but the PID estimator no longer has a full probabilistic interpretation and cannot be directly used to estimate the particle yields. One could iterate the probability distributions to determine the yields. Alternatively, one can build the PID estimator for each track independently, and an efficiency and migration must be determined for a given cut on the estimator value,  $P_{\text{track}} > P_{\text{cut}}$ . We will see that the necessary corrections are small and the systematic uncertainty is negligible compared to other sources, making this approach adequate. Second, we will consider the response functions of the different PID detectors as independent and can therefore factorize the probability into separate terms for the TOFW and CHE. Third, with the new detector hit selections, the time-of-flight and Cherenkov detector responses show no angular dependence allowing  $\theta$  to be removed from the above expression. Finally, we will only consider pions and protons as possible secondary particle types. Monte Carlo simulation shows other potential backgrounds to a  $\pi^+$  yield measurement to be small.

$$P(\alpha|\beta, N_{pe}, p) = \frac{P(\beta|\alpha, p) \cdot P(N_{pe}|\alpha, p)}{P(\beta, |\pi, p) \cdot P(N_{pe}|\pi, p) + P(\beta|p, p) \cdot P(N_{pe}|p, p)} \quad (5)$$

where  $P(\alpha|\beta, N_{pe}, p)$  is the PID estimator for a track with reconstructed  $\beta$ ,  $N_{pe}$  and  $p$  to be of type  $\alpha$  and  $P(\beta|p, p)$  and  $P(N_{pe}|p, p)$  are the response functions for the TOFW and CHE, respectively, which will be fully described below. Pions are selected by making a cut in this PID variable, equal to 0.6 in the present analysis.

The efficiency for pion selection and the migration between pions and protons can be calculated analytically from the parametrized detector response functions for a given cut in probability. These corrections consist (for each momentum bin) of a 2x2 matrix (PID efficiency matrix)

$$\begin{pmatrix} \pi \\ p \end{pmatrix}_{\text{rec}} = \begin{pmatrix} M_{\pi\pi} & M_{\pi p} \\ M_{p\pi} & M_{pp} \end{pmatrix} \cdot \begin{pmatrix} \pi \\ p \end{pmatrix}_{\text{true}} \quad (6)$$

where  $M_{\pi\pi}$  and  $M_{pp}$  are the efficiencies for correctly identifying pions and protons, respectively, and  $M_{\pi p}$  and  $M_{p\pi}$  are the migration terms of true protons identified as pions and true pions identified as protons, respectively. The full covariance matrix (16 terms) of the PID efficiency matrix is also computed analytically. This calculation is explained fully in [11]. The final expression for the PID efficiency-migration matrix elements reads:

$$M_{ij} = \sum_{S_c=0,1} C_j^{S_c} \cdot \left[ \int_{\beta_{\pi}^{S_c,0}}^{\infty, \beta_p^{S_c}} d\beta G_j(\beta) + \omega_j^{\pi p} \cdot S(P_i^{S_c} |_{\text{CHE}} > P_{\text{cut}}) \right] \quad (7)$$

where  $C_j^{S_c}$  is the Cherenkov efficiency (Fig. 15),  $G_j(\beta)$  and  $\omega_j^{\pi p}$  are the Gaussian (Fig. 12) and non-Gaussian contributions to the beta response, respectively, and  $S(P_i^{S_c} |_{\text{CHE}} > P_{\text{cut}})$  is a step function controlling the integration of the non-Gaussian part,  $\omega$ .

The 2x2 matrix of Eq. 6 is easily inverted for converting reconstructed yields into true yields of pions and protons. The elements of the matrix in Eq. 6 are shown in Fig. 16 as a function of particle momentum. The pion efficiencies are  $>95\%$  and the proton-pion migrations are all less than 1%. But first we must describe the detector response functions that are a key input to the efficiency and migration calculations.

## 6.2 PID detector hit selection and response functions

This section describes the quality criteria applied to select PID detector hits and the resulting response functions for pions and protons. Previously, PID detector hits have been associated with reconstructed tracks based only on a geometrical matching criterion. A Kalman filter package is used to extrapolate each track to the plane of each detector, and this position is compared to the reconstructed  $x, y$  positions of all reconstructed hits in that detector. The detector hit with the best matching  $\chi^2$  was then assigned to that track. In this scheme the reconstruction can associate a single detector hit with multiple tracks and each track likely has additional candidate detector hits which are being ignored. In particular, in [10] it was seen that a fraction of protons had a non-negligible amount of associated photo-electrons due to light from pions or electrons being wrongly associated with proton tracks. Also in [10] the TOFW response function contained a non-gaussian component where  $\approx 10\%$  of reconstructed  $\beta$  fell greater than  $5\sigma$  from the mean expectation and could not be used for identification. Additional criteria have been developed for selecting PID detector hits to address these issues and have led to a reduction in PID backgrounds by as much as a factor of 10 in some regions of phase space. This is the source of the drastic improvement in PID systematics since our previous publication (3.5% to 0.5%). The PID hit selection is described in detail below.

### 6.2.1 Time-of-flight response

A time-of-flight measurement is required for particle identification in this analysis. It was discovered, due to the presence of a significant, almost flat background far from the Gaussian peaks in the  $\beta$  distributions, that a more strict set of selection cuts was required to ensure a quality time-of-flight measurement. The small efficiency loss due to this selection can be measured directly from the data and will be combined with the tracking efficiency discussed above to form an overall reconstruction efficiency,

$$\epsilon^{\text{recon}} = \epsilon^{\text{track}} \cdot \epsilon^{\text{TOFW-match}}. \quad (8)$$

Each track can have multiple time-of-flight measurements ( $\text{TOFW} - t_0$ ) associated with it in the reconstruction. It is possible for a single hit to match with multiple tracks if the tracks are close enough together when hitting the wall. It is also possible that electromagnetic showers associated with a particle passing through detector material can create additional hits beyond the primary hit caused by the hadron of interest. To minimize inaccurate time measurements due to these effects, the

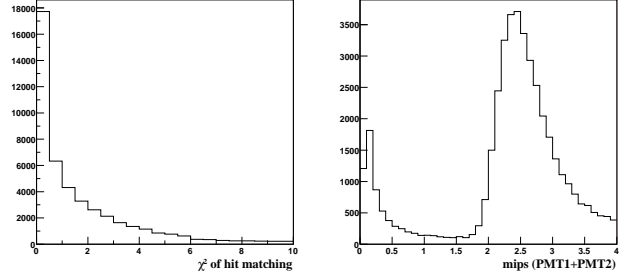


**Fig. 10.** TOFW hit reconstructed variables. The left panel shows the distribution of the  $\chi^2$  between the extrapolated track position and the reconstructed scintillator hit position. The right panel shows the total reconstructed number of minimum ionizing particles (mips) from the two PMTs on the scintillator volume that was hit. Time-of-flight hits are selected by requiring a  $\chi^2 \leq 6$  and number of mips  $\geq 1.5$  (see the text).

time-of-flight candidates for each track are time-ordered and the earliest hit passing the following criteria is selected:

- if the track shares the TOFW hit with another track, it must have the better geometric matching  $\chi^2$ ;
- $\chi^2$  of the geometrical matching between the track and TOFW hit  $\leq 6$ ;
- total reconstructed number of minimum ionizing particles (mips) from the two PMTs in a hit  $\geq 1.5$ .

The  $\chi^2$  distribution for track-TOFW hit matching and the total pulse-height distribution for this data set are shown in Fig. 10.

Having applied these criteria to time-of-flight measurements we must understand the associated efficiency loss as well as the remaining level of non-Gaussian component to the  $\beta$  spectrum. Each of these have been carefully measured and the needed corrections applied.

The efficiency is measured from the data by using a sample of reconstructed tracks which leave a signal in the calorimeter (downstream of the scintillator wall) and asking how often a time-of-flight measurement passing selection cuts is found. Fig. 11 shows the matching efficiency for data and Monte Carlo to be flat in momentum and around 95% in the data. This efficiency is combined with the tracking efficiency to provide the total analysis track reconstruction efficiency. The efficiencies generated from the data themselves have been used in the analysis for the results being presented here.

Having applied these selection criteria we must characterize the response of the time-of-flight detector for different particle types. The  $\beta$  response has been parameterized by a Gaussian function. A method has been developed to extract the parameters of this function directly from the data and has already been described in [10] and [11]. The method was applied to both data and Monte Carlo events and the results are shown in Fig. 12. The figure shows a small bias in the simulation of the time-of-flight resolution for protons above  $\approx 2$  GeV/c, resulting in a particle identification efficiency bias of about 0.5% (see Fig. 16). To avoid any bias introduced by the simulation of the time-of-flight system, the response functions as determined from data are used in the analysis of data.

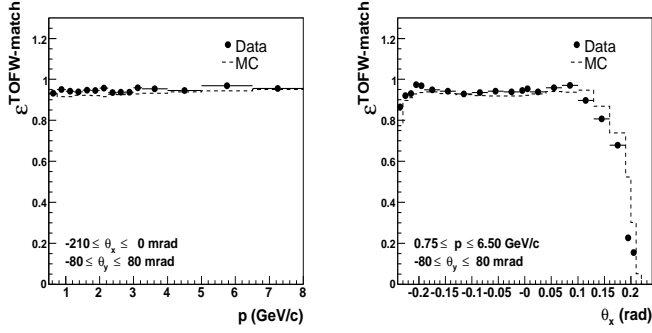


**Fig. 11.** TOFW matching efficiency as a function of particle momentum (left) and production angle in the horizontal plane,  $\theta_x$  (right) as measured from data and Monte Carlo. The TOFW matching efficiency does not have the momentum dependence of the tracking efficiency, but does exhibit the same effects of geometric acceptance as the drift chambers as seen in the right,  $\theta_x$ , plot. Note the present analysis is performed using tracks in the range  $-0.210 \text{ rad} \leq \theta_x \leq 0 \text{ rad}$  where the acceptance is flat in momentum.

Additionally, there is a small rate of non-Gaussian time-of-flight measurements, called " $\beta$ -outliers", which must be accounted for separately.  $\beta$ -outliers are defined as time-of-flight measurements greater than  $5\sigma$  from the mean of the expected  $\beta$  response function. This small, non-Gaussian component of the time-of-flight response, shown in Fig. 13, has been fully accounted for in the PID efficiency calculation described above. It should be noted that, due to the improvements in the hit selection criteria being described here, the  $\beta$ -outlier effect as described in [10] has been reduced from  $\sim 10\%$  to  $\sim 1\text{--}3\%$  since that publication. The outlier rate is the largest contribution to the systematic error coming from particle identification, and with this improvement PID now makes a negligible contribution to the total systematic error in the cross-section analysis.

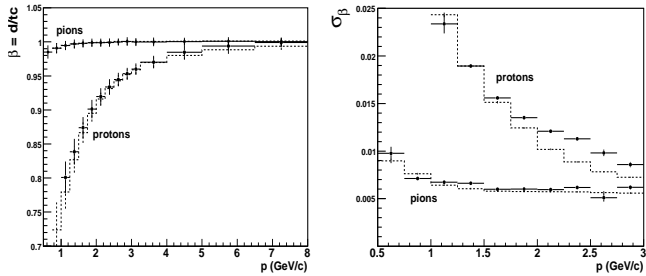


**Fig. 12.**  $\beta$  response for pions and protons as measured from data and Monte Carlo. The left panel shows the mean beta values with the error bars representing the width of the Gaussian distribution. The right panel highlights the width of the distributions and shows how the resolution asymptotically approaches  $\approx 0.006$ . The solid points are the response as measured from data; the dashed histograms are the response as measured from Monte Carlo.

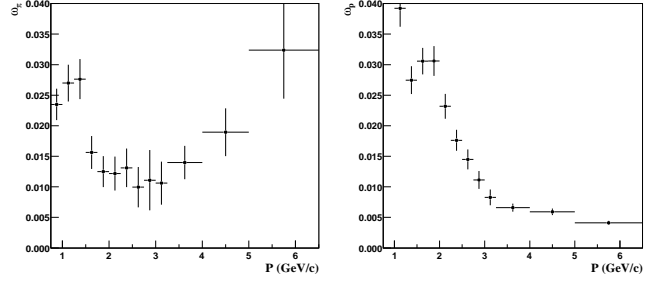


**Fig. 13.** Pion (left) and proton (right)  $\beta$ -outlier rates as a function of momentum. The pion outlier rate has been measured from the data; the proton outlier rate is estimated using the Monte Carlo. In reference [11] it has been demonstrated that no bias is seen when using the Monte Carlo to calculate the outlier rate.

## 6.2.2 Cherenkov response

The Cherenkov detector is used to veto electrons below 3 GeV/c and to differentiate pions from protons above 3 GeV/c.

Below 3 GeV/c the Cherenkov signal is not used in the calculation of the particle identification probability according to Eq. 5, but instead electrons are removed by a simple veto of tracks with greater than 15 photo-electrons. Fig. 14 demonstrates the effect of the electron veto cut. The left panel shows the  $e/\pi$  ratio in the Monte Carlo before and after applying the 15 photo-electron cut below 3 GeV/c. The remaining electron contamination is less than 1% everywhere, and less than 0.5% in the region where the veto is applied. One expects a very small efficiency loss for pions and protons due to this cut in photo-electrons and this is also shown in Fig. 14. Approximately 1% of pions and protons do not pass the electron veto; a correction has been applied in the present analysis.

Above 3 GeV/c the Cherenkov is a powerful discriminator of pions and protons. (Monte Carlo simulations indicate that there are a negligible number of electrons above 3 GeV/c and these are thus ignored.) Presently the Cherenkov is being used digitally. That is the spectral information of the light output is not being used. Instead we define a signal as an associated hit with greater than 2 photo-electrons. Two or less is considered no signal. Based on this definition we determine the efficiency for pions and protons to have a signal in the Cherenkov as a function of particle momentum. Fig. 15 shows the expected response for pions and protons in the Cherenkov both above and below the pion threshold. Above threshold the Cherenkov is greater than 99% efficient for pions. The small efficiency for protons and pions below threshold of around 1.5% is due to false associations with light generated by other particles in the event.

Using the characterized responses of the TOFW and CHE detectors we can calculate the PID estimator for reconstructed tracks given in Eq. 5 and the efficiency-migration matrix elements given by Eq. 7 and shown in Fig. 16.

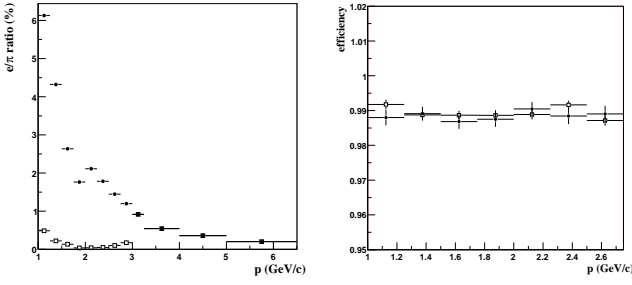


**Fig. 14.** The left panel shows the  $e/\pi$  ratio from a Monte Carlo simulation before (solid points) and after (open squares) the application of a 15 photo-electron cut. This cut reduces the electron contamination to 0.5% or less in the region where it is applied. The right panel shows the efficiency for pions (solid points) and protons (open squares) to pass the 15 photo-electron cut below 3 GeV/c, and is  $\approx 99\%$  for both.

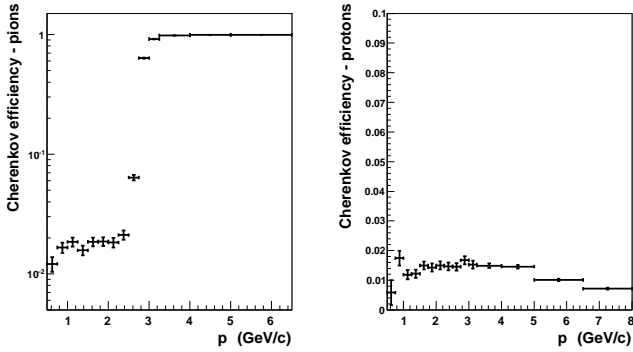


**Fig. 15.** Cherenkov response for pions (left) and protons (right). The points are the efficiencies for a track to have an associated Cherenkov hit with greater than 2 photo-electrons. The threshold for pions at around 2.6 GeV/c is clearly visible (note the log scale). The small efficiency for protons and below threshold pions of around 1.5% is due to false associations with light generated by other particles in the event.

## 7 Physics results

Applying corrections to the raw yields as described in the previous sections and according to Eq. 3, we have calculated the double-differential inelastic cross-section for the production of positive pions from collisions of 8.9 GeV/c protons with beryllium in the kinematic range from  $0.75 \text{ GeV}/c \leq p_\pi \leq 6.5 \text{ GeV}/c$  and  $0.030 \text{ rad} \leq \theta_\pi \leq 0.210 \text{ rad}$ .

Systematic errors have been estimated and will be described below. A full  $(13 \times 6)^2 = 6048$  element covariance matrix has been generated to describe the correlation among bins. The data are presented graphically as a function of momentum in 30 mrad angle bins in Fig. 17 and 1D projections onto the momentum and angle axes are shown in Fig. 18. The central values and square-root of the diagonal elements of the covariance matrix are listed in Table 5.

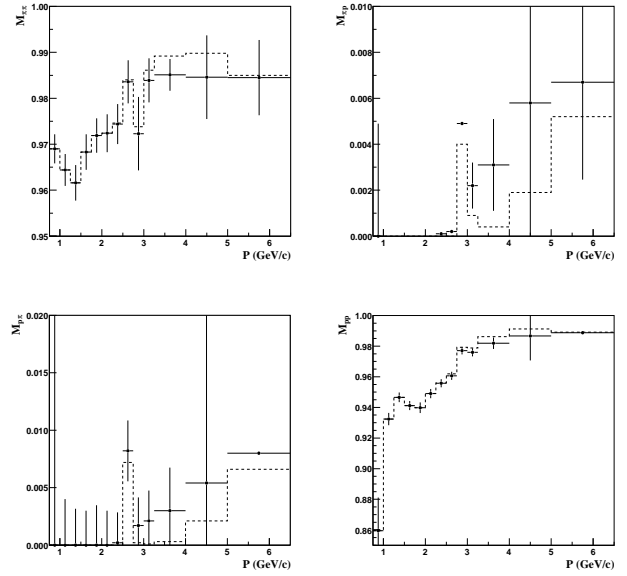


**Fig. 16.** Particle ID efficiency and migration matrix elements as a function of momentum. Upper left is the pion identification efficiency,  $M_{\pi\pi}$ . Upper right is the proton to pion migration,  $M_{\pi p}$ . Lower left is the pion to proton migration,  $M_{p\pi}$ . Lower right is the proton identification efficiency,  $M_{pp}$ . Points with errors are the values calculated from data. The dashed histograms are those determined from the Monte Carlo. The slight data-Monte Carlo bias seen above 2.5 GeV/c results from the bias seen in the TOFW simulation. The values determined from data have been used in the analysis to avoid sensitivity to this bias.

### 7.1 Error estimation

A full systematic error evaluation has been performed on these data in order to estimate the accuracy of the measurement being presented. Statistical errors from both the beryllium target data and the 8.9 GeV/c empty target data set used to subtract non-target backgrounds are also included.

The uncertainties associated with the various corrections applied have been estimated through a combination of analytical and Monte Carlo techniques. The approach used here has largely followed the methods of [10]. There are eight sources of systematic uncertainty considered which can be grouped into three basic categories: track yield corrections, PID, and momentum reconstruction.

Only the PID uncertainties have been calculated analytically. The covariance matrices of the PID efficiency-migration matrices described in Sec. 6 have been calculated and the errors propagated. The cross-section uncertainties from the other sources are estimated by performing the cross-section calculation  $N$  times for  $N$  variations of each correction applied. The fully correlated error matrix for each correction is then built from the  $N$  cross-section results,

$$E_{ij}^\alpha = \frac{1}{N} \sum_{n=1}^N \left[ \frac{d^2\sigma_{\text{CV}}^\pi}{dpd\Omega} - \frac{d^2\sigma_{\alpha,n}^\pi}{dpd\Omega} \right]_i \times \left[ \frac{d^2\sigma_{\text{CV}}^\pi}{dpd\Omega} - \frac{d^2\sigma_{\alpha,n}^\pi}{dpd\Omega} \right]_j \quad (9)$$

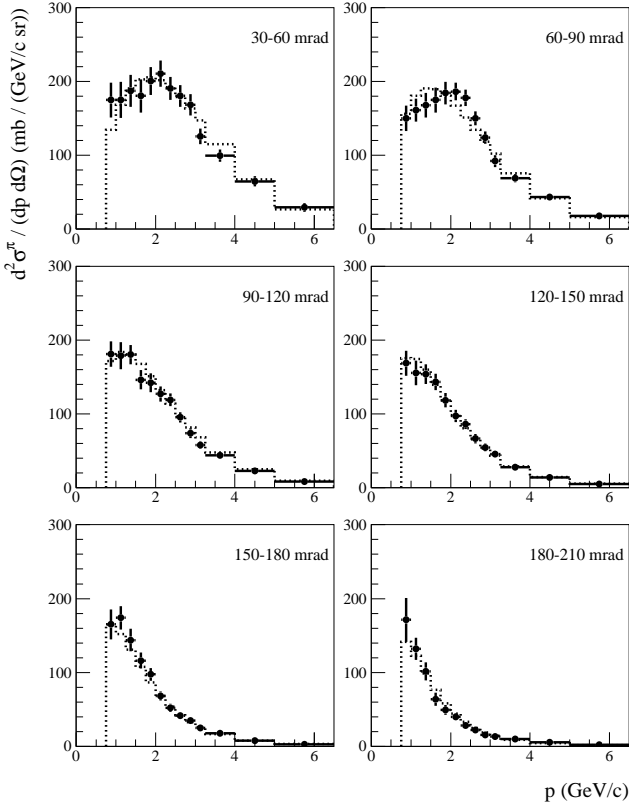


**Fig. 17.** Measurement of the double-differential production cross-section of positive pions,  $d^2\sigma^{\pi^+}/dpd\Omega$ , from 8.9 GeV/c protons on beryllium as a function of pion momentum,  $p$ , in bins of pion angle,  $\theta$ , in the laboratory frame. The error bars shown include statistical errors and all (diagonal) systematic errors. The dotted histograms show the extended Sanford-Wang parametrization of Eq. 14 with parameter values given in Table 3.

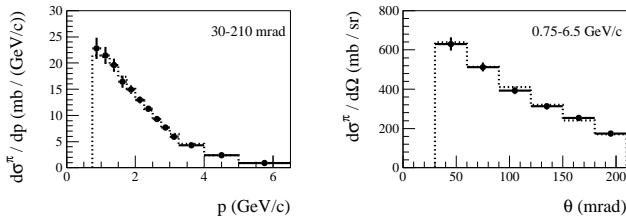


**Fig. 18.** Projections of the double-differential cross-section results onto the momentum axis integrated over the angular range  $30 \text{ mrad} \leq \theta < 210 \text{ mrad}$  (left) and onto the angle axis integrated over the momentum range  $0.75 \text{ GeV}/c \leq p < 6.5 \text{ GeV}/c$  (right). Projections for the best-fit extended Sanford-Wang parametrization are also shown, as indicated by dotted histograms.

where  $i$  and  $j$  label bins of  $(p, \theta)$ ,  $E_{ij}^\alpha$  is the  $i, j^{th}$  element of one of the error matrices (labeled  $\alpha$ ),  $d^2\sigma_{CV}^\pi/(dpd\Omega)$  is the central value for the double-differential cross-section measurement and  $d^2\sigma_{\alpha,n}^\pi/(dpd\Omega)$  is the cross-section result from the  $n^{th}$  variation for the  $\alpha^{th}$  systematic. For example, to estimate the cross-section uncertainty arising from the absorption correction, 100 analyses are performed where only the absorption correction is randomly fluctuated 100 times with an RMS of 10%. This 10% is the uncertainty of the absorption correction as described in Sec. 4.4. The total error matrix is just the sum of the  $\alpha$  matrices,  $E_{ij} = \sum_\alpha E_{ij}^\alpha$ .

The full  $78 \times 78$  elements of the covariance matrix will not be published here, but to characterize the uncertainties on this measurement we show the square-root of the diagonal elements of the covariance matrix plotted on the data points in Fig. 17. Fig. 19 shows the fractional uncertainty (again diagonal) for each  $(p, \theta)$  bin. The total error as well as the contributions from statistical errors, track yield corrections and momentum reconstruction are shown. Additionally, we define a dimensionless quantity,  $\delta_{\text{diff}}$ , expressing the typical diagonal error on the double-differential cross-section

$$\delta_{\text{diff}} \equiv \frac{\sum_i E_{ii}}{\sum_i (d^2\sigma_{CV}^\pi/(dpd\Omega))_i} \quad (10)$$

We also define the fractional error on the total integrated pion cross-section in the range of the measurement ( $0.75 \text{ GeV}/c \leq p < 6.5 \text{ GeV}/c$ ,  $30 \text{ mrad} \leq \theta < 210 \text{ mrad}$ ),  $\delta_{\text{int}}$ :

$$\delta_{\text{int}} \equiv \frac{\sqrt{\sum_{i,j} (dpd\Omega)_i E_{ij} (dpd\Omega)_j}}{\sum_i (d^2\sigma^\pi)_i}, \quad (11)$$

where  $(d^2\sigma^\pi)_i$  is the double-differential cross-section in bin  $i$ ,  $(d^2\sigma^\pi/(dpd\Omega))_i$ , multiplied by its corresponding phase space element  $(dpd\Omega)_i$ .  $E_{ij}$  is the covariance matrix evaluated for the double-differential cross-section data.

For example, the 30%–40% absorption correction (see Fig. 5) with a 10% uncertainty results in an average diagonal error of 3.6% on the cross-section, as one expects. The uncertainty on the integrated cross-section is approximately the same since this correction is a fully correlated yield adjustment.

Table 2 summarizes these quantities for each of the various error sources considered with a typical total uncertainty of 9.8% on the double-differential cross-section values being reported and a 4.9% uncertainty on the total integrated cross-section.

## 7.2 Parametrization of pion production data

Sanford and Wang [16] have developed an empirical parametrization for describing the production cross-sections of mesons in proton-nucleus interactions. This parametrization has the functional form:

$$\frac{d^2\sigma(p+A \rightarrow \pi^+ + X)}{dpd\Omega}(p, \theta) = \exp[A] p^{c_2} \left(1 - \frac{p}{p_{\text{beam}}}\right), \quad (12)$$

Error Category	Comment on method for estimating error	$\delta_{\text{diff}}^{\pi}$ (%)	$\delta_{\text{int}}^{\pi}$ (%)
Statistical Errors:			
Be target statistics	statistical error	4.2	0.6
Empty target subtraction	statistical error	4.6	0.6
<b>Sub-total</b>		<b>6.3</b>	<b>0.8</b>
Track yield corrections:			
Reconstruction efficiency	stat of tracking efficiency computation sample	1.3	0.8
Pion, proton absorption	10% uncertainty on $\pi$ , p absorption rates	3.6	3.7
Tertiary subtraction	50% uncertainty on tertiary production rate	1.8	1.8
Empty target subtraction	5% uncertainty on empty target subtraction normalization	1.3	1.2
<b>Sub-total</b>		<b>4.6</b>	<b>4.3</b>
Particle Identification:			
Electron veto	stat of electron veto efficiency computation sample	0.2	<0.1
Pion, proton ID correction	analytical propagation of errors from parameterized PID detector response functions as described in [11]	0.4	0.1
<b>Sub-total</b>		<b>0.5</b>	<b>0.1</b>
Momentum reconstruction:			
Momentum scale	2% uncertainty on absolute momentum scale	3.6	0.1
Momentum resolution	different hadronic generators used to generate correction	3.4	1.0
<b>Sub-total</b>		<b>5.2</b>	<b>1.0</b>
Overall normalization:	targeting eff., fully correlated recon. and PID contributions	<b>2.0</b>	<b>2.0</b>
<b>Total</b>		<b>9.8</b>	<b>4.9</b>

**Table 2.** Summary of the uncertainties affecting the double-differential cross-section ( $\delta_{\text{diff}}$ ) and integrated cross-section ( $\delta_{\text{int}}$ ) measurements (defined in text).

where:

$$A = c_1 - c_3 \frac{p^{c_4}}{p_{\text{beam}}^{c_5}} - c_6 \theta (p - c_7 p_{\text{beam}} \cos^{c_8} \theta), \quad (13)$$

and  $X$  denotes any system of other particles in the final state,  $p_{\text{beam}}$  is the proton beam momentum in GeV/c,  $p$  and  $\theta$  are the  $\pi^+$  momentum and angle in units of GeV/c and radians, respectively,  $d^2\sigma/(dpd\Omega)$  is expressed in units of mb/(GeV/c)/sr,  $d\Omega \equiv 2\pi d(\cos\theta)$ , and the parameters  $c_1, \dots, c_8$  are obtained from fits to meson production data.

The parameter  $c_1$  is an overall normalization factor, the four parameters  $c_2, c_3, c_4, c_5$  describe the momentum distribution of the secondary pions in the forward direction, and the three parameters  $c_6, c_7, c_8$  describe the corrections to the pion momentum distribution for pion production angles that are different from zero.

The  $\pi^+$  production data reported here have been fitted to the empirical Sanford-Wang formula. In the  $\chi^2$  minimization procedure, seven out of these eight parameters were allowed to vary. The parameter  $c_5$  was fixed to the conventional value  $c_5 \equiv c_4$ , since the cross-section dependence on the proton beam momentum cannot be addressed by the present HARP data-set, which includes exclusively measurements taken at  $p_{\text{beam}} = 8.9$  GeV/c. In the  $\chi^2$  minimization, the full error matrix was used. The goodness-of-fit of the Sanford-Wang parametrization hypothesis for the HARP results can be assessed by considering the best-fit  $\chi^2$  value of  $\chi_{\text{min}}^2 = 248$  for 71 degrees of freedom, indicating a very poor fit quality. In particular, inspection of the HARP inclusive pion production double-differential cross-section, and resulting Sanford-Wang parametrization,

points to a description of the ratio  $g(\theta)$  of the pion momentum distribution at  $\theta \neq 0$  with respect to the  $\theta = 0$  pion momentum distribution that is more complicated than what can be accommodated within the Sanford-Wang formula, where this ratio is given by  $g(\theta) = \exp[-c_6\theta(p - p_c)]$ , with  $p_c \equiv c_7 p_{\text{beam}} \cos^{c_8} \theta$ .

Given the poor description of this HARP pion production data-set in terms of the original Sanford-Wang parametrization, we explored alternative functional forms. We found a significantly better representation of the data by adopting a simple generalization of the Sanford-Wang formula, obtained by introducing one extra-parameter  $c_9 \neq 0$  for the description of the angular dependence of the pion momentum distribution, according to  $g(\theta) = (1 + p/p_{\text{beam}})^{c_9\theta(p-p_c)} \exp[-c_6\theta(p - p_c)]$ . Overall, we use the following parametrization for the inclusive  $\pi^+$  production double-differential cross-section:

$$\frac{d^2\sigma}{dpd\Omega}(p, \theta) = \exp[A] p^{c_2} \left(1 - \frac{p}{p_{\text{beam}}}\right) \times \left(1 + \frac{p}{p_{\text{beam}}}\right)^{c_9\theta(p - c_7 p_{\text{beam}} \cos^{c_8} \theta)}, \quad (14)$$

where the argument  $A$  in the exponent is given by Eq. 13. We obtain in this case a best-fit  $\chi^2$  value of  $\chi_{\text{min}}^2 = 117$  for 70 degrees of freedom.

Concerning the parameters estimation, the best-fit values of the extended Sanford-Wang parameter set discussed above are reported in Table 3, together with their errors. The fit parameter errors are estimated by requiring  $\Delta\chi^2 \equiv \chi^2 - \chi_{\text{min}}^2 = 9.30$ , corresponding to the 68.27% confidence level region for eight



Parameter	Value
$c_1$	$(5.13 \pm 0.41)$
$c_2$	$(1.87 \pm 0.52)$
$c_3$	$(6.67 \pm 1.69)$
$c_4 = c_5$	$(1.56 \pm 0.55)$
$c_6$	$(1.19 \pm 0.18) \cdot 10^1$
$c_7$	$(1.73 \pm 0.31) \cdot 10^{-1}$
$c_8$	$(1.98 \pm 0.69) \cdot 10^1$
$c_9$	$(1.60 \pm 0.44) \cdot 10^1$

**Table 3.** Extended Sanford-Wang parameters and errors obtained by fitting the dataset. The errors refer to the 68.27% confidence level for eight parameters ( $\Delta\chi^2 = 9.30$ ).

Parameter	$c_1$	$c_2$	$c_3$	$c_4 = c_5$	$c_6$	$c_7$	$c_8$	$c_9$
$c_1$	1.000							
$c_2$	0.341	1.000						
$c_3$	0.099	0.562	1.000					
$c_4 = c_5$	-0.696	-0.730	0.004	1.000				
$c_6$	-0.309	0.288	0.735	0.358	1.000			
$c_7$	-0.609	0.066	-0.221	0.030	0.005	1.000		
$c_8$	-0.170	-0.030	-0.270	-0.173	-0.433	0.672	1.000	
$c_9$	-0.250	0.270	0.819	0.368	0.973	-0.060	-0.393	1.000

**Table 4.** Correlation coefficients among the extended Sanford-Wang parameters, obtained by fitting the data.

variable parameters. Significant correlations among fit parameters are found, as shown by the correlation matrix given in Table 4.

The HARP cross-section measurement is compared to the best-fit parametrization of Eqs. 14 and 13, and Table 3, in Figs. 17 and 18. Also by looking at Fig. 17, one can qualitatively conclude that the proposed generalization of the Sanford-Wang parametrization provides a reasonable description of the data spectral features over the entire pion phase space measured. On the other hand, as already noted in [10], we remark that the goodness-of-fit depends on the correlations among the HARP cross-section uncertainties in different  $(p, \theta)$  bins, and therefore cannot be inferred solely from Fig. 17.

We defer to a later publication, which should include a more comprehensive study of  $\pi^+$  production at various beam momenta and from various nuclear targets, a more complete discussion on the adequacy of parametrization-driven models such as Sanford-Wang (or simple modifications of) to describe HARP hadron production data.

## 8 Relevance of HARP beryllium results for neutrino experiments

The Booster neutrino beam at the Fermi National Accelerator Laboratory in Batavia, Illinois is created from the decay of charged mesons passing through a 50 m open decay region. These mesons are produced when 8.9 GeV/c momentum protons are impinged upon a 71 cm long  $(1.7\lambda)$  by 1 cm diameter beryllium target located at the upstream end of a magnetic focusing horn. This neutrino beam has been used by the MiniBooNE experiment since September, 2002 and will be used by the SciBooNE experiment starting in summer, 2007.

The MiniBooNE (E898) experiment at Fermilab [4] was designed to address the yet unconfirmed oscillation signal reported by the LSND collaboration [6]. MiniBooNE has been searching for the appearance of electron neutrinos in a beam that is predominantly muon flavor with an  $L/E$  similar to LSND but with substantially differing systematics. Additionally, the MiniBooNE detector can be used to make neutrino interaction cross-section measurements for both charged-current and neutral-current processes. An important systematic for these analyses arises from the prediction of the fluxes of different neutrino flavors at the MiniBooNE detector. For the  $\nu_e$  appearance search the effect of the normalization uncertainty on  $\pi^+$  production is largely reduced by a constraint provided by the *in situ* measurement of  $\nu_\mu$  charged-current quasi-elastic events. Neutrino cross-section measurements at MiniBooNE, however, will directly benefit from reductions in neutrino flux normalization uncertainties enabled by these hadron data.

The neutrino flux prediction at the MiniBooNE detector is generated using a Monte Carlo simulation implemented in Geant4 [15]. Primary meson production rates are presently determined by fitting the empirical parametrization of Sanford and Wang [16] to production data in the relevant region. The results presented here, being for protons at exactly the Booster beam energy, are a critical addition to the global Sanford-Wang parametrization fits.<sup>3</sup>

A flux prediction based on these data has been used by the MiniBooNE collaboration in their search for  $\nu_e$  appearance at  $\Delta m^2 \sim 1 \text{ eV}^2$  [5]. The systematic uncertainty on their pre-

<sup>3</sup> Cross-section data from the Brookhaven E910 experiment are also used to provide an additional constraint to the Sanford-Wang formula at angles larger than 210 mrad. These data are from 6.4 and 12.3 GeV/c proton beams on a beryllium target.

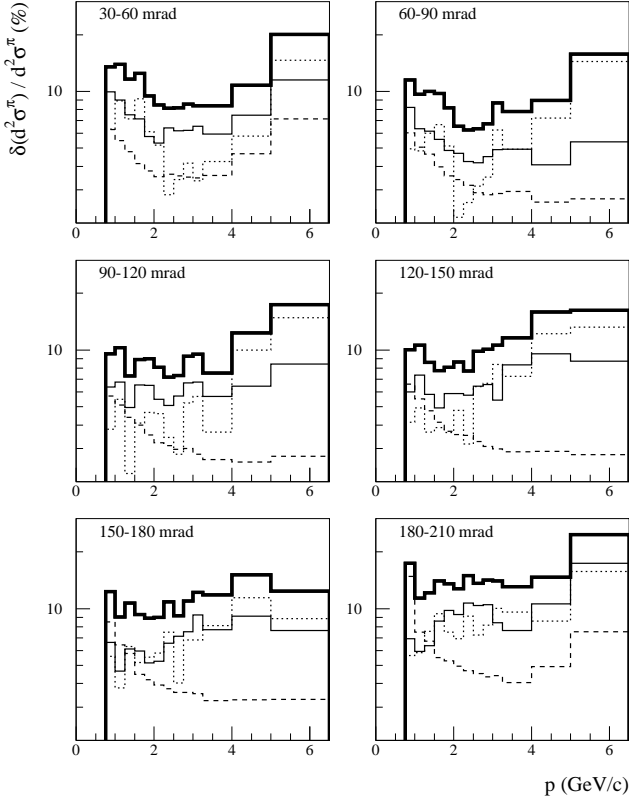


**Fig. 19.** Fractional uncertainty (in percent) on the double-differential pion production cross-section measured, as a function of pion momentum and angle. The total uncertainty is shown by the thick black histograms, and individual contributions from the error categories given in Tab. 2 are also shown. Statistical, track yield corrections, and momentum reconstruction uncertainties are shown as thin solid, dashed, and dotted histograms, respectively; the overall normalization uncertainty is not shown, and the particle identification uncertainty contribution lies below 2% for all pion momenta and angles.

diction of  $\nu_e$  from  $\pi^+ \rightarrow \mu^+ \rightarrow \nu_e$  as a background to the oscillation analysis is 8% [5] with only a 3% contribution from the  $\pi^+$  production model based on these data. In contrast, the uncertainty on the prediction of  $\nu_e$  from kaon decays is 35% [5], the largest contribution (25%) coming from the production model of kaons in p+Be interactions, also based on parameterizations of available cross-section data.

Using the complete MiniBooNE beam Monte Carlo we can illustrate the direct impact of the HARP data on the MiniBooNE flux predictions. The dominant channel leading to a muon neutrino in the detector is  $p + \text{Be} \rightarrow \pi^+ \rightarrow \nu_\mu$ . Fig. 20 shows the total  $\nu_\mu$  flux (solid) according to the simulation as well as the part coming directly from the sequence listed above (dashed). The curves are obtained from a Geant4 simulation of the Booster Neutrino Beam at Fermilab based on the parametrization of the HARP  $\pi^+$  production cross-section given in Eqs. 12 and 13 and Table 3. Figure 21 shows the kinematic distribution of  $\pi^+$ 's which result in a  $\nu_\mu$  in the MiniBooNE detector. The box outlines the kinematic range of the measurements described in this paper. The simulation indicates that  $>80\%$  of the relevant pions

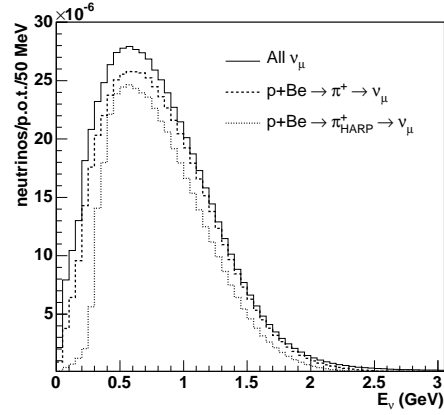


**Fig. 20.** Predicted muon neutrino flux at the MiniBooNE detector from a Geant4 simulation of the Booster Neutrino Beam at Fermilab based on the parametrization of the HARP  $\pi^+$  production cross-section (Eqs. 12 and 13 and Table 3). The solid curve is the total muon neutrino flux, while the dashed curve is the part of the  $\nu_\mu$  flux coming from the decay of  $\pi^+$  created in proton-beryllium collisions. The primary production of positive pions is based on a parametrization of the HARP  $\pi^+$  cross-section measurements presented in this paper and represents the predominant source of  $\nu_\mu$  at MiniBooNE. The dotted histogram shows the part of the  $\nu_\mu$  flux coming from the decay of  $\pi^+$ 's that are within the kinematic boundaries of the measurement presented here,  $0.75 \text{ GeV}/c \leq p_\pi \leq 6.5 \text{ GeV}/c$  and  $0.030 \text{ rad} \leq \theta_\pi \leq 0.210 \text{ rad}$ .

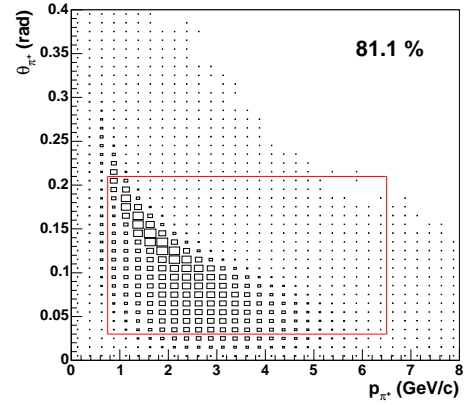


**Fig. 21.**  $p$ - $\theta$  distribution of  $\pi^+$ 's which decay to a muon neutrino passing through the MiniBooNE detector according to a Monte Carlo simulation. The box marks the kinematic region of the measurement presented here and contains 81.1% of the pions contributing to the neutrino flux at MiniBooNE.

come from within this region. The neutrinos produced by the subset of pion phase-space directly covered by this measurement are shown by the dotted histogram in Fig. 20. While the coverage of these data is being displayed for the MiniBooNE detector, a similar coverage is expected for the SciBooNE detector [9] located in the same neutrino beam at Fermilab.

## 9 Summary and conclusions

In this paper we have presented a measurement of the double-differential production cross-section of positive pions in the collision of 8.9 GeV/c protons with a beryllium target. The data have been reported in 78 bins of pion momentum and angle in the kinematic range from  $0.75 \text{ GeV}/c \leq p_\pi \leq 6.5 \text{ GeV}/c$  and  $0.030 \text{ rad} \leq \theta_\pi \leq 0.210 \text{ rad}$ . A systematic error analysis has been performed yielding an average point-to-point error of 9.8% (statistical + systematic) and an uncertainty on the total integrated cross-section of 4.9%. Further, the data have been fitted to a modified form of the empirical parameterization of Sanford and Wang and the resulting parameters provided.

These production data have direct relevance for the prediction of a  $\nu_\mu$  flux for MiniBooNE, an experiment searching for  $\nu_\mu \rightarrow \nu_e$  oscillations using the Booster neutrino beam line at Fermi National Accelerator Laboratory, and SciBooNE, an experiment designed to measure  $\nu_\mu$  cross-sections in the 1 GeV neutrino energy region using the same beam. Final flux predictions for these experiments will be based on the results presented here and published elsewhere by the MiniBooNE and SciBooNE collaborations.

## 10 Acknowledgments

We gratefully acknowledge the help and support of the PS beam staff and of the numerous technical collaborators who contributed to the detector design, construction, commissioning and operation. In particular, we would like to thank G. Barichello, R. Brocard, K. Burin, V. Carassiti, F. Chignoli, D. Conventi, G. Decreuse, M. Delattre, C. Detraz, A. Domeniconi, M. Dwuznik, F. Evangelisti, B. Friend, A. Iacofano, I. Krasin, D. Lacroix, J.-C. Legrand, M. Lobello, M. Lollo, J. Loquet, F. Marinilli, J. Mulon, L. Musa, R. Nicholson, A. Pepato, P. Petev, X. Pons, I. Rusinov, M. Scandurra, E. Usenko, and R. van der Vlugt, for their support in the construction of the detector. The collaboration acknowledges the major contributions and advice of M. Baldo-Ceolin, L. Linssen, M.T. Muciaccia and A. Pulia during the construction of the experiment. The collaboration is indebted to V. Ableev, F. Bergsma, P. Binko, E. Boter, M. Calvi, C. Cavion, A. Chukanov, M. Doucet, D. Düllmann, V. Ermilova, W. Flegel, Y. Hayato, A. Ichikawa, A. Ivanchenko, O. Klimov, T. Kobayashi, D. Kustov, M. Laveder, M. Mass, H. Meinhard, A. Menegolli, T. Nakaya, K. Nishikawa, M. Pasquali, M. Placentino, S. Simone, S. Troquereau, S. Ueda and A. Valassi for their contributions to the experiment.

We acknowledge the contributions of F. Dydak and J. Wotschack to the work described in this paper.

We are indebted to the MiniBooNE collaboration who made available their beam-line simulation for the calculation of the predicted neutrino fluxes at their detector.

The experiment was made possible by grants from the Institut Interuniversitaire des Sciences Nucléaires and the Interuniversitair Instituut voor Kernwetenschappen (Belgium), Ministerio de Educacion y Ciencia, Grant FPA2003-06921-c02-02 and Generalitat Valenciana, grant GV00-054-1, CERN (Geneva, Switzerland), the German Bundesministerium für Bildung und Forschung (Germany), the Istituto Nazionale di Fisica Nucleare (Italy), INR RAS (Moscow) and the Particle Physics and

Astronomy Research Council (UK). We gratefully acknowledge their support.

## References

1. E. Aliu *et al.* [K2K Collaboration], “Evidence for muon neutrino oscillation in an accelerator-based experiment,” *Phys. Rev. Lett.* **94**, 081802 (2005) [arXiv:hep-ex/0411038].
2. M. H. Ahn *et al.* [K2K Collaboration], “Measurement of neutrino oscillation by the K2K experiment,” *Phys. Rev. D* **74** (2006) 072003 [arXiv:hep-ex/0606032].
3. Y. Ashie *et al.* [Super-Kamiokande Collaboration], “A measurement of atmospheric neutrino oscillation parameters by Super-Kamiokande I,” *Phys. Rev. D* **71** (2005) 112005 [arXiv:hep-ex/0501064].
4. E. Church *et al.* [BooNE Collaboration], “A proposal for an experiment to measure muon-neutrino  $\rightarrow$  electron-neutrino oscillations and muon-neutrino disappearance at the Fermilab Booster: BooNE”, FERMILAB-PROPOSAL-0898.
5. A. A. Aguilar-Arevalo *et al.* [The MiniBooNE Collaboration], “A search for electron neutrino appearance at the  $\Delta m^2 \sim 1 - eV^2$  scale,” arXiv:0704.1500 [hep-ex].
6. A. Aguilar *et al.* [LSND Collaboration], “Evidence for neutrino oscillations from the observation of anti- $\nu_e$  appearance in a anti- $\nu_\mu$ /mu beam”, *Phys. Rev. D* **64** (2001) 112007 [arXiv:hep-ex/0104049].
7. M. G. Catanesi *et al.* [HARP Collaboration], “The HARP Detector at the CERN PS”, *Nucl. Instrum. Meth. A* **571** (2007) 527.
8. M. Anfreville *et al.*, “The drift chambers of the NOMAD experiment”, *Nucl. Instrum. Meth. A* **481** (2002) 339. [arXiv:hep-ex/0104012].
9. A. A. Aguilar-Arevalo *et al.* [SciBooNE Collaboration], “Bringing the SciBar detector to the Booster neutrino beam”, [arXiv:hep-ex/0601022].
10. M. G. Catanesi *et al.* [HARP Collaboration], “Measurement of the production cross-section of positive pions in p Al collisions at 12.9-GeV/c”, *Nucl. Phys. B* **732** (2006) 1 [arXiv:hep-ex/0510039].
11. M. G. Catanesi *et al.* [HARP Collaboration], “Particle identification algorithms for the HARP forward spectrometer”, *Nucl. Instrum. Meth. A* **572** (2007) 899.
12. M. Baldo-Ceolin *et al.*, “The Time-Of-Flight TOFW Detector Of The HARP Experiment: Construction And Performance”, *Nucl. Instrum. Meth. A* **532** (2004) 548.
13. G. Folger, V. N. Ivanchenko, J. P. Wellisch, “The Binary cascade”, *Eur. Phys. Jour. A21* (3) (2004) 407.
14. A. Heikkinen, N. Stepanov and J. P. Wellisch, “Bertini intra-nuclear cascade implementation in Geant4,” In the Proceedings of 2003 Conference for Computing in High-Energy and Nuclear Physics (CHEP 03), La Jolla, California, 24-28 Mar (2003), pp MOMT008 [arXiv:nucl-th/0306008].
15. S. Agostinelli *et al.* [GEANT4 Collaboration], “GEANT4: A simulation toolkit”, *Nucl. Instrum. Meth. A* **506** (2003) 250.
16. J. R. Sanford and C. L. Wang, “Empirical formulas for particle production in p-Be collisions between 10 and 35 BeV/c”, Brookhaven National Laboratory, AGS internal report, (1967) (*unpublished*).

$\theta_{\min}$ (mrad)	$\theta_{\max}$ (mrad)	$p_{\min}$ (GeV/c)	$p_{\max}$ (GeV/c)	$d^2\sigma^{\pi^+}/(dpd\Omega)$ (mb/(GeV/c sr))	
30	60	0.75	1.00	174.7	$\pm 23.6$
		1.00	1.25	174.8	$\pm 24.4$
		1.25	1.50	187.2	$\pm 21.7$
		1.50	1.75	180.2	$\pm 22.5$
		1.75	2.00	200.3	$\pm 18.9$
		2.00	2.25	210.5	$\pm 17.8$
		2.25	2.50	190.4	$\pm 15.5$
		2.50	2.75	180.2	$\pm 14.7$
		2.75	3.00	168.4	$\pm 14.4$
		3.00	3.25	125.3	$\pm 10.5$
		3.25	4.00	99.1	$\pm 8.3$
60	90	4.00	5.00	64.4	$\pm 6.9$
		5.00	6.50	29.2	$\pm 5.9$
		0.75	1.00	150.1	$\pm 17.2$
		1.00	1.25	161.1	$\pm 15.5$
		1.25	1.50	167.8	$\pm 16.7$
		1.50	1.75	174.6	$\pm 17.0$
		1.75	2.00	184.1	$\pm 15.0$
		2.00	2.25	186.2	$\pm 12.1$
		2.25	2.50	177.4	$\pm 11.1$
		2.50	2.75	149.7	$\pm 9.5$
		2.75	3.00	123.6	$\pm 8.3$
90	120	3.00	3.25	92.0	$\pm 8.0$
		3.25	4.00	68.8	$\pm 5.4$
		4.00	5.00	43.2	$\pm 3.9$
		5.00	6.50	17.5	$\pm 2.8$
		0.75	1.00	180.7	$\pm 17.3$
		1.00	1.25	178.8	$\pm 18.4$
		1.25	1.50	180.2	$\pm 13.1$
		1.50	1.75	146.1	$\pm 13.0$
		1.75	2.00	142.2	$\pm 12.8$
		2.00	2.25	126.9	$\pm 10.3$
		2.25	2.50	118.8	$\pm 8.5$
120	150	2.50	2.75	95.2	$\pm 7.0$
		2.75	3.00	73.8	$\pm 6.8$
		3.00	3.25	57.9	$\pm 5.5$
		3.25	4.00	43.7	$\pm 3.3$
		4.00	5.00	22.9	$\pm 2.8$
		5.00	6.50	8.3	$\pm 1.5$
		0.75	1.00	168.7	$\pm 16.9$
		1.00	1.25	155.3	$\pm 16.5$
		1.25	1.50	153.7	$\pm 13.2$
		1.50	1.75	142.9	$\pm 11.1$
		1.75	2.00	118.4	$\pm 9.6$
150	180	2.00	2.25	97.1	$\pm 8.4$
		2.25	2.50	86.0	$\pm 6.6$
		2.50	2.75	66.4	$\pm 6.5$
		2.75	3.00	54.6	$\pm 5.5$
		3.00	3.25	45.2	$\pm 4.8$
		3.25	4.00	27.6	$\pm 3.2$
		4.00	5.00	13.5	$\pm 2.2$
		5.00	6.50	4.9	$\pm 0.8$
		0.75	1.00	165.2	$\pm 20.3$
		1.00	1.25	173.9	$\pm 15.7$
		1.25	1.50	143.8	$\pm 15.4$
180	210	1.50	1.75	116.1	$\pm 10.8$
		1.75	2.00	97.4	$\pm 8.6$
		2.00	2.25	68.2	$\pm 6.1$
		2.25	2.50	52.1	$\pm 5.6$
		2.50	2.75	41.5	$\pm 3.8$
		2.75	3.00	35.0	$\pm 3.8$
		3.00	3.25	24.8	$\pm 3.0$
		3.25	4.00	17.4	$\pm 2.1$
		4.00	5.00	7.8	$\pm 1.2$
		5.00	6.50	2.8	$\pm 0.3$
		0.75	1.00	171.3	$\pm 29.8$
210		1.00	1.25	131.9	$\pm 15.0$
		1.25	1.50	101.6	$\pm 12.3$
		1.50	1.75	63.5	$\pm 8.9$
		1.75	2.00	49.2	$\pm 6.7$
		2.00	2.25	39.7	$\pm 5.1$
		2.25	2.50	28.1	$\pm 4.2$
		2.50	2.75	21.8	$\pm 3.0$
		2.75	3.00	15.6	$\pm 2.2$
		3.00	3.25	13.1	$\pm 1.8$
		3.25	4.00	9.9	$\pm 1.3$
		4.00	5.00	5.6	$\pm 0.8$
240		5.00	6.50	1.8	$\pm 0.4$

**Table 5.** HARP results for the double-differential  $\pi^+$  production cross-section in the laboratory system,  $d^2\sigma^{\pi^+}/(dpd\Omega)$ . Each row refers to a different ( $p_{\min} \leq p < p_{\max}, \theta_{\min} \leq \theta < \theta_{\max}$ ) bin, where  $p$  and  $\theta$  are the pion momentum and polar angle, respectively. The central value as well as the square-root of the diagonal elements of the covariance matrix are given.

